Journal of Sound and Vibration (1997) **200**(5), 665–699

NOISE FROM SUPERSONIC COAXIAL JETS, PART 2: NORMAL VELOCITY PROFILE

M. D. Dahl

National Aeronautics and Space Administration, Lewis Research Center, Cleveland, OH 44135, *U.S.A.*

AND

P. J. Morris

Department of Aerospace Engineering, The Pennsylvania State University, University Park, PA 16802, *U.S.A.*

(*Received* 5 *February* 1996, *and in final form* 19 *August* 1996

Instability waves have been established as noise generators in supersonic jets. Recent analysis of these slowly diverging jets has shown that these instability waves radiate noise to the far field when the waves have components with phase velocities that are supersonic relative to the ambient speed of sound. This instability wave noise generation model has been applied to supersonic jets with a single shear layer and is now applied to supersonic coaxial jets with two initial shear layers. In this paper the case of coaxial jets with normal velocity profiles is considered, where the inner jet stream velocity is higher than the outer jet stream velocity. To provide mean flow profiles at all axial locations, a numerical scheme is used to calculate the mean flow properties. Calculations are made for the stability characteristics in the coaxial jet shear layers and the noise radiated from the instability waves for different operating conditions with the same total thrust, mass flow and exit area as a single reference jet. The effects of changes in the velocity ratio, the density ratio and the area ratio are each considered independently.

1. INTRODUCTION

Since the beginning of jet aircraft transportation service, community noise created by jet exhausts has been a problem. Increased awareness of noise pollution has hampered the expansion of service from using predominantly subsonic aircraft to including more supersonic aircraft. To lessen the community noise problem, many experimental and theoretical studies have been performed to increase the understanding of the jet noise generation process, particularly of those processes that are important to supersonic jet noise. Basic understanding leads to means by which the noise generation process may be modified and acceptable community noise levels provided from supersonic jet aircraft.

In this paper a method to modify the noise generating mechanism in supersonic jets is examined. A single, axisymmetric jet is replaced by a dual stream, coaxial jet. The two jet streams have different initial velocities and possibly different initial temperatures. The jets are classified as having a normal velocity profile (NVP) if the inner stream velocity is higher than the outer stream velocity and as having an inverted velocity profile (IVP) if the inner stream velocity is less than that of the outer stream. This paper concentrates on NVP supersonic jets. IVP supersonic jets are discussed in a companion paper [1].

0022–460X/97/100665 + 35 $18.00/0/sv960724

1.1. NVP COAXIAL JET NOISE

The interest in the measurement of the noise radiated from coaxial jets increased as the by-pass jet engine was introduced as an alternative propulsion system to the noisy turbojet engine. Early results as to whether or not any variation in the outer stream velocity had any affect on the radiated noise were inconclusive [2]. With the consensus that the noise reduction in by-pass engines was due to lower velocities at the same mass flow compared to single jets, measurements were later made of noise reduction in cold coaxial subsonic jets at constant thrust [3]. It was found that, by adding an annular outer stream U_2 to the axisymmetric inner stream U_1 and reducing U_1 while increasing U_2 to maintain constant thrust, the maximum noise reduction occurred at about $U_2/U_1 = 1$ compared to the noise generated by the inner jet alone. In effect, the jet exit area was increased and the jet velocity decreased. Alternatively, by simply increasing the outer velocity U_2 for a fixed inner velocity U_1, the maximum noise reduction occurred at a velocity ratio of 0·5. This apparent noise reduction was confirmed by others [4, 5]. In addition, reductions were noted in high frequency noise, including the peak of the jet noise spectrum, but there was an increase in low frequency noise [5]. Olsen and Friedman [6] conducted a wide ranging study of coaxial nozzles and flow conditions. Their results showed minimum noise levels at velocity ratios of 0·4–0·5, with variations apparently due to changing area ratios. Thus, for subsonic jets, there appeared to be lower noise benefits in using coaxial jets with normal velocity profiles.

In the early studies of NVP coaxial jets, different methods of comparison were used to quantify the amount of noise reduction that was achieved using a two-stream jet. This led to confusion as to what exactly were the benefits of using coaxial jets. In order to provide a rational basis for comparison and to clarify the previous jet measurement data, Tanna [7] re-examined some of the normal velocity profile data, discussed earlier, and compared the results to a reference jet at the same thrust, mass flow and exit area. His conclusion was simply that subsonic NVP coaxial jets, with both inner stream velocity and temperature greater than the outer stream, are noisier than the reference jet. A systematic study of subsonic NVP jets confirmed this conclusion [8]. Given the constraint of constant exit area, one stream will always have a velocity higher than the reference jet in order to maintain constant total thrust and mass flow. Since the maximum velocity of a normal profile jet persists longer than the maximum velocity of the single reference jet then, in a Lighthill sense, the NVP jet will generate more noise than the reference jet.

Experimental work on coaxial jets was also conducted in the supersonic flow regime [9]. Using converging nozzles, the jets were operated above the critical pressure ratio, resulting in underexpanded, shock-containing flows. A minimum noise condition was defined based on overall sound pressure level measurements at upstream angles at which shock associated noise dominates. For a fixed outer nozzle pressure ratio above critical, minimum noise was found when the inner nozzle pressure ratio was slightly above critical, at about 1·9. Depending on the initial velocities and temperatures of the two jet streams, this condition was found to hold for jets with both inverted velocity profiles and normal velocity profiles.

With the shock associated noise virtually eliminated and schlieren photographs showing the destruction of the outer jet repetitive shock structure at minimum noise conditions, the remaining mixing noise at downstream angles to the jet axis was measured [9]. Test conditions of constant thrust, mass flow and exit area, along with the added condition that the inner stream be slightly supersonic to achieve minimum noise due to shocks, were used to set the coaxial jet initial velocities and temperatures. As was found for shock-free coaxial jets, normal velocity profile jets were noisier than the reference jet based on overall sound pressure level measurements at 30 degrees to the jet axis.

Much of the data from the reports discussed above has been used to develop models for predicting noise radiation from coaxial jets. Noise measurements from different nozzles at different conditions provided data for empirical models [10–12] and correlations [13]. A more theoretical approach based on turbulence modelling and Lighthill's independent noise producing eddies was proposed [14]. A turbulence model was used in calculating mean flow properties, which were the only quantities needed for the acoustic calculations. In a more elaborate approach, turbulence modelling was used to predict both mean flow and turbulence variables [15–17]. With a model for the acoustic source of an elemental jet volume based on local turbulence properties, these results were used in Lilley's equation to predict far field radiated noise levels and spectra. These models tend to agree favorably with measured data since they all contain factors that were derived from measured data. As an alternative to these models, we calculate noise radiation from instability waves propagating in the shear layers of supersonic coaxial jets.

1.2. INSTABILITY WAVES IN NVP JETS

In supersonic jets, instability waves have been established as a dominant source of mixing noise [18]. These waves, generated by the instability of the jet shear layer, radiate noise when they have phase velocities that are supersonic relative to ambient conditions. Initially, both shear layers will support growing instability waves. As the shear layers grow and merge together, the growth rates and phase velocities of these instability waves will be modified by this process.

Studies have been conducted of the existence of large scale structures or instability waves in subsonic NVP coaxial jets [19–21]. Using microphones and hot wires to measure pressure and velocity fluctuations, the presence of large scale structures was inferred in both shear layers of the developing coaxial jet. As expected, the large scale structures in both shear layers rotated in the same direction as those large structures found in a single jet. Spectral measurements were made for various velocity ratios U_2/U_1. As measurements were made in the radial direction, the peak in the spectrum shifted from being associated with the inner shear layer to being associated with the outer shear layer as the velocity ratio increased. The inner shear layer had the dominant spectral peak when $U_2/U_1 < 0{\cdot}5$ and the outer shear layer had the dominant spectral peak when $U_2/U_1 \geqslant 0{\cdot}5$. As the measurements proceeded downstream to the fully developed jet, the dominant shear layer peak was the one that continued to exist. A smaller peak due to large scale structures in the smaller shear layer disappeared, indicating that those structures decayed more rapidly. Further examination of the spectral data showed that for $U_2/U_1 < 0{\cdot}5$ the dominant inner shear layer peak had a higher frequency than the outer shear layer peak. This was due to the higher convection velocity for the large scale structures in the inner shear layer compared to that in the outer shear layer. When $U_2/U_1 > 0{\cdot}5$, ΔU across the outer shear layer is larger than that across the inner shear layer resulting in a dominant low frequency peak in the spectrum. This peak is due to the lower convection velocity for the large structures in the outer shear layer than in the inner shear layer.

Instead of relying on indirect measurements, a flow visualization study was conducted of low speed, incompressible, coaxial jets in order to reveal the large scale structures in the two shear layers [22]. The development of the instabilities into large scale structures and their interaction as they evolved downstream was observed in each shear layer. A wide variety of patterns was observed in the jet near field as the velocity ratio and the absolute velocity were varied, with a fixed area ratio of 0·94 and density ratio of 1·0. For a velocity ratio of $0{\cdot}59 \leqslant U_2/U_1 < 1$, the largest scale structures in the outer shear layer dominated the flow dynamics, with only small instabilities seen in the inner shear layer. It was noted in the study that, near a velocity ratio equal to one, wake-like instabilities were a factor

in the flow dynamics. They had a greater impact on the flow development when the wake was thinner and had a larger velocity deficit. At velocity ratios less than one, the instabilities due to the wake quickly disappeared in favour of shear layer instabilities as the velocity profile smoothed out.

Since large scale structures are modelled as instability waves, the local stability characteristics for the shear layers in a coaxial jet can be calculated in the same manner as the calculations are performed for single jets. A first attempt to do this was conducted by Bhat and Seiner [23] for supersonic coaxial jets. The mean flow was described analytically and it was known in the core region only. For the NVP jet with $U_2/U_1 = 0{\cdot}52$, the outer shear layer stability characteristics were found to be similar to the equivalent single jet stability characteristics. These results were in agreement with the trends observed from the measured low speed coaxial jet data discussed above. However, because the mean flow was not known beyond the end of the potential core region, the complete growth and decay of the instability waves could not be obtained. The methodology that we follow allows us to complete the growth and decay description of the instability waves in supersonic coaxial jets and, subsequently, to calculate the radiated noise.

1.3. THEORETICAL CONSIDERATIONS

With the instability waves established as noise generators in supersonic jets when they have phase velocities that are supersonic relative to ambient, the mixing noise radiated from these waves when the jet is perfectly expanded has a directivity pattern with a dominant peak in the downstream arc of the jet. Even when shocks are present in the jet flow, the noise from the jet that radiates into the downstream arc is primarily due to mixing, whereas the broadband noise associated with shocks dominates in the upstream arc of the jet. Extensive measurements have shown this for single jets [24] and for coaxial jets [25]. Hence, to a first approximation, we could conduct an analysis of the mixing noise in the region in which it dominates, even if shocks were present in the flow. However, since this is a first analysis of the instability wave nose generation model in supersonic coaxial jets, we assume that the coaxial jets are perfectly expanded or, if not, that the jet operating conditions are set for minimum noise where the flow has the characteristics of perfect expansion downstream of a composite shock structure near the nozzle. This simplifies the analysis and allows us to concentrate on profile shaping as a means of further reducing the mixing noise. Many of the ideas behind this analytical approach are given in Tam and Burton [26] and Tam [18]. These references refer to single axisymmetric jets and they contain detailed comparisons between predictions and measurements of both flow and acoustic properties. Here, we use these ideas in the extension of this approach to mixing noise generation from supersonic coaxial jets.

In the analysis, the jet flow is decomposed into three parts: the mean flow, large scale structures and fine scale turbulence. The equations of motion for each of these components may be derived formally from the full equations of motion if it is assumed that there is a sufficient separation of length and time scales between the large and small scale unsteady motions. To proceed further, additional simplifying assumptions are required. First, it is assumed that the gross properties of the large scale structures are controlled by weakly non-linear mechanisms. Experimental observations in excited free shear flows indicate that this is a good approximation, at least for the growing part of the structure's evolution: see, for example, Gaster *et al*. [27] for the two-dimensional shear layer and Petersen and Samet [28] for the circular jet. Unsteady flow models have been developed for the excited jet [29] and for the two-dimensional shear layer [30], based on this weakly non-linear assumption. In these models it is noted that the large scale structures are quasi-periodic in both space and time. Therefore, their properties are naturally, not just mathematically,

described well by a wave-like form. This is consistent with their equations of motion being locally linear. Further arguments to support the weakly non-linear nature of the growing large scale structures are given in the appendix to Morris *et al*. [30].

As the large structures evolve in the axial direction, they extract energy from the mean flow. From energy considerations, this causes the mean width of the jet shear layer to increase. Predictions have been made to support the hypothesis that it is this process that is the most important in the mean flow development in a two-dimensional shear and the annular mixing region of a jet [30]. The details of the mechanisms by which the large scale structures or instability waves transfer their energy to smaller scale motions is unimportant, as far as the gross development of the mean flow is concerned. This process is not well understood, but the details are likely to be highly non-linear. In the instability wave model used here, for the noise generation and radiation process, it is assumed that the interaction or energy transfer between the large and small scales may be described by an eddy viscosity model. The value of this eddy viscosity should be much smaller than the value used in Part 1 of this paper [31] to model the effects of turbulence on the development of the mean flow, since the latter includes effects of both the large and small scale motions. Thus the equivalent turbulent Reynolds number will be high. At high Reynolds number for free shear flows, the inviscid and viscous solutions of the equations of motion are very similar. Thus, as a final simplification, we assume that the decay of the large scale structures may also be modelled by an inviscid approximation: as long as the inviscid analysis is the correct limit for the infinite Reynolds number. This is discussed in more detail below. It is acknowledged that this is a crude model for a complicated process; however, the evidence from single axisymmetric jets indicates that it does not have a significant effect on the noise predictions. Furthermore, in the present study of coaxial jets, we have emphasized relative changes in the noise radiation due to changes in operating conditions, rather than absolute predictions. Therefore, absolute accuracy and the precise modelling of all details of the turbulent flow are not essential.

The instability waves in the inviscid model are inflectional instabilities of the Kelvin–Helmholtz type. They have been shown to be the dominant instabilities in the jets

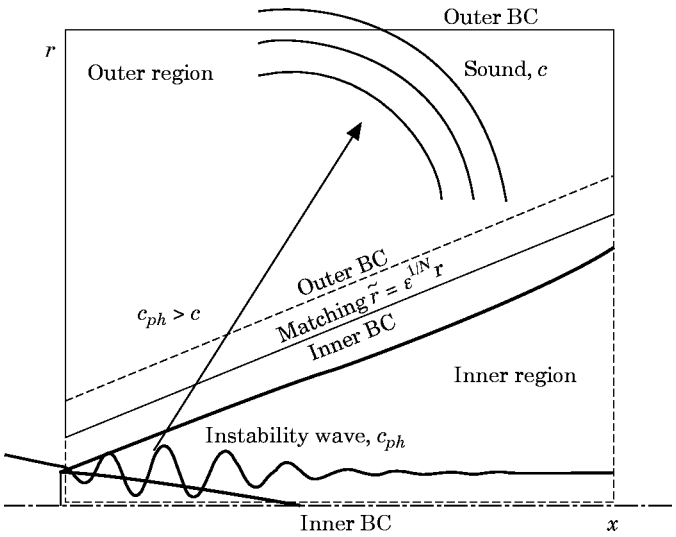

Figure 1. A schematic illustrating the inner (r, $s = \varepsilon x$) and outer ($\bar{r} = \varepsilon r$, $s = \varepsilon x$) regions of the matched asymptotic solution. The inner region including the jet flow is outlined by a thin dashed line (– – – –). The outer region is outlined by a thin solid line (———) outside the jet.

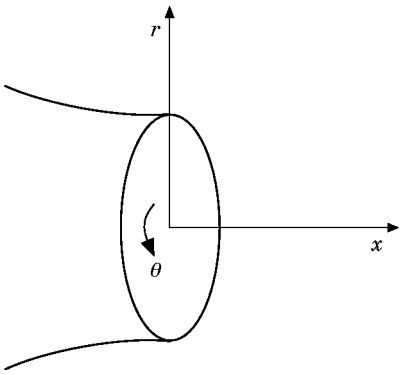

Figure 2. The cylindrical co-ordinate system centered on the nozzle exit.

of interest in this paper [32, 33]. As shown in Tam and Hu [34], there are other waves traveling in the shear layer that have subsonic and supersonic phase velocities. In the inviscid limit, the Kelvin–Helmholtz waves are analytically continued from growing to damped waves. These other waves become neutrally stable without viscosity and do not become damped downstream. Since they do not contribute to peak noise, they are not considered here. The damped Kelvin–Helmholtz waves are found for both subsonic and supersonic phase velocities [35]. The full analysis for the instability wave noise generation model involves a large amount of algebraic manipulation. In this paper an outline of the solution is provided. Many additional details may be found in Burton [36]. Tam and Burton [26] and Dahl [37].

The analytical and numerical analysis provided the means by which to conduct a parametric study of supersonic coaxial jets. We chose a reference single stream jet with operating conditions that would be typical for a supersonic transport aircraft engine exhaust. From these conditions, we defined the operating conditions for supersonic coaxial jets that have the same total thrust, total mass flow and total exit area as the reference jet. The study of normal velocity profile jets allowed variations in the velocity ratio, the density ratio and the area ratio between the two jet streams to be controlled separately. Thus, for example, the variation in the velocity ratio could be studied with the density and area ratios fixed.

2. THE INSTABILITY WAVE AND SOUND FIELD SOLUTION

In this section the theory that governs the development of the instability waves in supersonic jets and their identification as sources of noise radiated to the far field is outlined. The formulation follows the approach of Tam and Burton [26] with the addition of a non-zero free stream velocity [38]. Solutions are created that apply to separate but overlapping regions, as illustrated in Figure 1. In the inner region, equations are developed that apply to the slowly diverging jet and its immediate environs. After a multiple scales expansion, the result to lowest order is a description of the instability wave in terms of its local growth rate and phase speed. Next, the outer solution is developed after rescaling the governing equations, since the disturbances in the outer region are acoustic in nature and they travel in all directions with equal length scales. This is followed by the matching process, where the inner and outer regions overlap, that completes the description of the instability wave to lowest order. We then present expressions for the near field pressure fluctuations and the far field directivity pattern. Finally, after describing the numerical

procedures used to complete the calculations, we verify our procedures for numerical accuracy and compare our numerically calculated results to analytical calculations for single and coaxial jets.

2.1. LINEARIZED EQUATIONS OF MOTION

The linearized equations of motion for small disturbances are derived from the following compressible, inviscid equations of motion:

continuity,
$$\frac{\partial \rho}{\partial t} + \nabla \cdot (\rho \mathbf{V}) = 0; \tag{1}$$

momentum,
$$\rho\left[\frac{\partial \mathbf{V}}{\partial t} + \mathbf{V} \cdot \nabla \mathbf{V}\right] = -\nabla p; \tag{2}$$

energy,
$$\frac{\partial p}{\partial t} + \mathbf{V} \cdot \nabla p + \gamma p \nabla \cdot \mathbf{V} = 0; \tag{3}$$

where equation (3) is derived by combining the continuity equation and the state equation for a perfect gas to eliminate the enthalpy from the original energy equation. These equations have been non-dimensionalized by the following reference values: spatial co-ordinates by R_1, time by R_1/U_1, velocity by U_1, density by ρ_1, and pressure by $\rho_1 U_1^2$. The subscript 1 is used to indicate jet exit conditions for a single jet or for the inner stream of a coxial jet.

To linearize these equations we let

$$\rho = \bar{\rho} + \rho', \qquad \mathbf{V} = \bar{\mathbf{V}} + \mathbf{V}', \qquad p = \bar{p} + p', \tag{4}$$

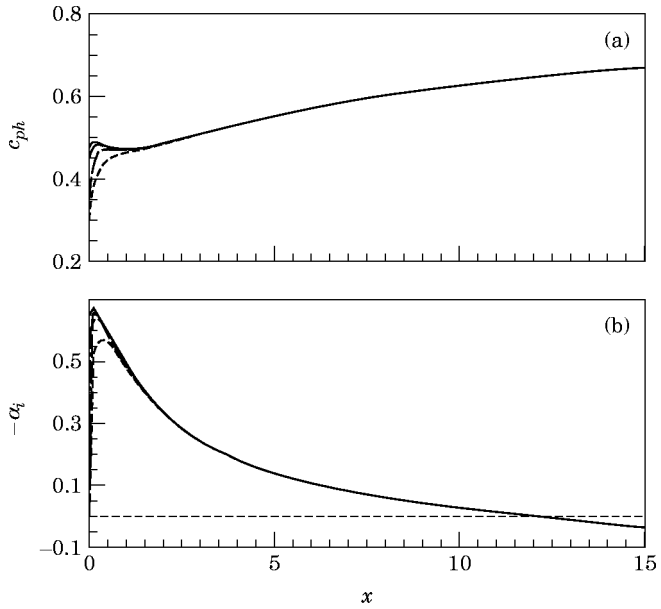

Figure 3. Results for the local stability calculations at four different radial grid spacings: $n = 1$; $fD_1/U_1 = 0{\cdot}2$. ----, $\Delta r = 0{\cdot}008$, $N = 250$; — — —, $\Delta r = 0{\cdot}004$, $N = 500$; — - — -, $\Delta r = 0{\cdot}002$, $N = 1000$; ———, $\Delta = 0{\cdot}001$, $N = 2000$. (a) Phase velocity; (b) growth rate.

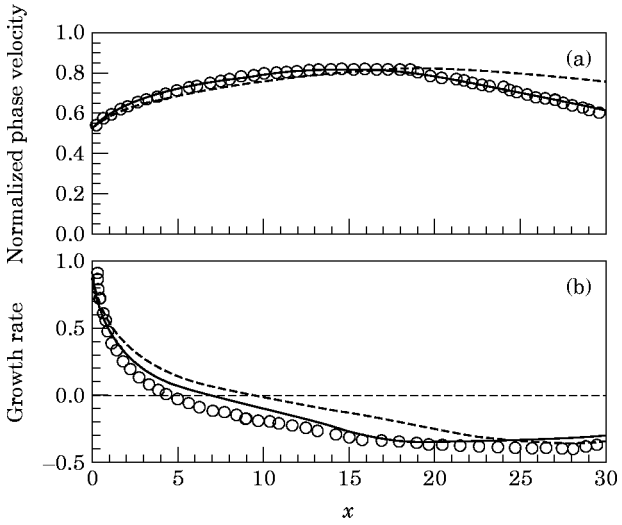

Figure 4. A comparison of results from the stability calculations for a single jet: $n = 1$, $fD_1/U_1 = 0{\cdot}4$. ----, Calculated results using numerically generated mean flow as defined in Part 1 of this paper [31]; ———, calculated results using numerically generated mean flow modified to match potential core length of measured data; ○, calculated results from reference [33] for mean flow defined with analytic functions. (a) Phase velocity; (b) growth rate.

where the overbar denotes a mean flow quantity and the prime denotes a fluctuating quantity; in this case, a small amplitude instability wave. Let us substitute equations (4) into equations (1), (2), and (3). After expanding terms, subtracting the equations governing the mean flow quantities, and neglecting higher order terms containing products of fluctuating quantities, we get the linearized equations.

$$\frac{\partial \rho'}{\partial t} + \bar{\mathbf{V}} \cdot \nabla \rho' + \mathbf{V}' \cdot \nabla \bar{\rho} + \bar{\rho} \nabla \cdot \mathbf{V}' + \rho' \nabla \cdot \bar{\mathbf{V}} = 0, \tag{5}$$

$$\frac{\partial \mathbf{V}'}{\partial t} + \bar{\mathbf{V}} \cdot \nabla \mathbf{V}' + \mathbf{V}' \cdot \nabla \bar{\mathbf{V}} + \frac{\rho'}{\bar{\rho}} [\bar{\mathbf{V}} \cdot \nabla \bar{\mathbf{V}}] = -\frac{1}{\bar{\rho}} \nabla p', \tag{6}$$

$$\frac{\partial p'}{\partial t} + \bar{\mathbf{V}} \cdot \nabla p' + \gamma \bar{p} \nabla \cdot \mathbf{V}' + \gamma p' \nabla \cdot \bar{\mathbf{V}} = 0. \tag{7}$$

These equations have included the conditions that the mean flow is steady and that, for a free jet, the mean static pressure is constant throughout the flow. Taking into consideration that the mean pressure is non-dimensional and constant, it is easy to show that $\gamma \bar{p} = 1/M_1^2$, where M_1 is the jet exit Mach number.

2.2. INNER SOLUTION TO LOWEST ORDER

A cylindrical co-ordinate system centered on the nozzle exit, as shown in Figure 2, is used for axisymmetric jets. The cylindrical co-ordinates (r, θ, x) have corresponding velocities (v, w, u). For supersonic jets, the mean flow changes slowly in the axial direction and is represented by [26]

$$\bar{\mathbf{V}} = (\varepsilon\bar{v}_1(r, x), 0, \bar{u}(r, x)). \tag{8}$$

Outside the jet, as $r \to \infty$, the ambient mean flow conditions are

$$\bar{\mathbf{V}} = \bar{\mathbf{V}}_\infty = \left(\varepsilon\frac{\bar{v}_\infty}{r}, 0, \bar{u}_\infty\right), \qquad \bar{\rho} = \bar{\rho}_\infty. \tag{9}$$

The ε in equation (8) represents the rate of spread of the jet mixing layer, which is small for supersonic jets and, hence, ε is the small parameter of the problem.

To construct the inner solution, we transform the axisymmetric co-ordinate (r, x) to (r, s), where $s = \varepsilon x$ is the slow co-ordinate. The fluctuating disturbances are then represented as an asymptotic series of waves travelling through a non-uniform medium, which in this case is the mean flow of the jet [26, 39]. For example, the fluctuating pressure disturbance is

$$p'(r, \theta, x\, t) = \sum_{m=0}^{\infty} \delta_m(\varepsilon)\hat{p}_m(r, s) \exp\left[\mathrm{i}\left(\frac{\phi(s)}{\varepsilon} + n\theta - \omega t\right)\right], \tag{10}$$

where $\phi(s)$ is an axial phase function and $\delta_m(\varepsilon)$ is the gauge function with $\delta_0(\varepsilon) = 1$, and the higher order terms, $m > 0$, have functional forms for $\delta_m(\varepsilon)$ that are found from the asymptotic expansion of the outer solution in the matching process.

After writing the linearized equations (5)–(7) of continuity, motion and energy, in cylindrical co-ordinates, transforming to the (r, s) co-ordinates and applying the expansion represented by equation (10), we partition the equations into terms according to $\delta_m(\varepsilon)$, combine the set of equations in favor of $\hat{p}_m$ and cast the resulting equation into the form

$$\frac{\partial^2\hat{p}_m}{\partial r^2} + \left[\frac{1}{r} + \frac{2\alpha}{\omega - \alpha\bar{u}}\frac{\partial\bar{u}}{\partial r} - \frac{1}{\bar{\rho}}\frac{\partial\bar{\rho}}{\partial r}\right]\frac{\partial\hat{p}_m}{\partial r} + \left[\bar{\rho}M_1^2(\omega - \alpha\bar{u})^2 - \frac{n^2}{r^2} - \alpha^2\right]\hat{p}_m = G_m(r, s), \tag{11}$$

where α is the axial wavenumber related to the axial phase function $\phi(s)$ in equation (10) by $\mathrm{d}\phi/\mathrm{d}s = \alpha(s)$. The right side term G_m depends on lower order terms only. To lowest order, $m = 0$, G_0 is zero and the equation is homogeneous. The homogeneous form of equation (11) is commonly called the compressible Rayleigh equation.

Outside the jet, equation (11) reduces, for $\hat{p}_0$, to

$$\frac{\partial^2\hat{p}_0}{\partial r^2} + \frac{1}{r}\frac{\partial\hat{p}_0}{\partial r} + \left[\bar{\rho}_\infty M_1^2(\omega - \alpha\bar{u}_\infty)^2 - \frac{n^2}{r^2} - \alpha^2\right]\hat{p}_0 = 0. \tag{12}$$

Equation (12) is Bessel's equation, with a solution of the form

$$\hat{p}_0 = A_0\mathrm{H}_n^{(1)}(\mathrm{i}\lambda r) + B_0\mathrm{H}_n^{(2)}(\mathrm{i}\lambda r). \tag{13}$$

The functions $\mathrm{H}_n^{(1)}$ and $\mathrm{H}_n^{(2)}$ are the nth order Hankel functions of the first and second kind, respectively, and

$$\lambda(\alpha) = [\alpha^2 - \bar{\rho}_\infty M_1^2(\omega - \alpha\bar{u}_\infty)^2]^{1/2}. \tag{14}$$

The branch cuts for equation (14) are chosen to ensure that the function decays for large r. It can be shown that the complex value of $\lambda(\alpha)$ must be in the range

$$-\pi/2 \leqslant \arg\lambda(\alpha) \leqslant \pi/2. \tag{15}$$

To generalize, the lowest order solution of equation (11) has two linearly independent solutions ζ_1^p and ζ_2^p that are functions of r and s. The amplitudes of these functions will vary with axial location, giving a solution of the form

$$\hat{p}_0(r, s) = A_0(s)\zeta_1^p(r, s) + B_0(s)\zeta_2^p(r, s). \tag{16}$$

As $r \to \infty$, equation (16) must be equivalent to equation (13), and as $r \to 0$, $\hat{p}_0$ must be finite.

2.3. OUTER SOLUTION

In the region outside the jet, the ambient conditions $\bar{\rho}_\infty$ and $\bar{u}_\infty$ are uniform. Disturbances that travel in this region are independent of the co-ordinate system. Hence, distances travelled by the disturbance in any direction will be of the same scale. Using the cylindrical co-ordinate system of the inner solution, the axial co-ordinate was rescaled as $s = \varepsilon x$. To bring the radial co-ordinate in the outer region to the same scale, we let $\bar{r} = \varepsilon r$ be the scaled radial co-ordinate.

To obtain the outer equations, we substitute equation (9) into equations (5), (6) and (7), transform them from the (r, x) co-ordinates to the $(\bar{r}, s)$ co-ordinates, and apply the azimuthal and time dependencies $\exp(\mathrm{i}n\theta - \mathrm{i}\omega t)$.

The solution to the outer equations is found by taking the Fourier transform of the disturbance variables converting from the spatial variable s to the transform variable k. For instance, the Fourier transform pair for the pressure disturbances is as follows:

Fourier transform;
$$\tilde{p}(k) = \frac{1}{2\pi}\int_{-\infty}^{\infty} p'(s)\, \mathrm{e}^{-\mathrm{i}ks}\, \mathrm{d}s; \tag{17}$$

inverse Fourier transform;
$$p'(s) = \int_{-\infty}^{\infty} \tilde{p}(k)\, \mathrm{e}^{\mathrm{i}ks}\, \mathrm{d}k; \tag{18}$$

After applying the transform, we arrange the equations and combine them to obtain a single equation in terms of the transformed disturbance velocity $\tilde{u}$. That equation can be transformed into the form of a Bessel equation, the right side of which is non-zero but very small [26]. We then obtain an approximate solution, valid to order ε^2,

$$\tilde{u} \sim C y^{q/2} \mathrm{H}_q^{(1)}(\mathrm{i}\xi y^{1/2}), \tag{19}$$

where

$$y = \bar{r}^2 - \varepsilon^4 \bar{\rho}_\infty M_1^2 \bar{v}_\infty^2, \qquad a = -\mathrm{i}\varepsilon \bar{\rho}_\infty M_1^2(\omega - \varepsilon k \bar{u}_\infty)\bar{v}_\infty,$$

$$\xi^2 = \frac{1}{\varepsilon_2}(\varepsilon^2 k^2 - \bar{\rho}_\infty M_1^2(\omega - \varepsilon k \bar{u}_\infty)^2), \qquad q^2 = n^2 - \varepsilon^2 \bar{\rho}_\infty^2 M_1^4(\omega - \varepsilon k \bar{u}_\infty)^2 \bar{v}_\infty^2,$$

and $\mathrm{H}_q^{(1)}$ is a Hankel function of the first kind of order q, that satisfies the outgoing wave or boundedness condition as $\bar{r} \to \infty$. The factor C may be found from the inner boundary condition for the outer transformed velocity $\tilde{u}$ as $y \to 0$ and $\bar{r} \to 0$. As suggested by Figure 1, the source of the disturbances outside the jet is the instability wave. Thus, the outer disturbance velocity $u'(\bar{r}, s)$ must converge towards the inner disturbance velocity as the outer solution approaches the inner boundary condition for the outer region. In essence, the inner boundary condition for $u'(\bar{r}, s)$ has the instability waveform suggested by equation (10) [40]. At this point, the form of the inner boundary condition is generalized by some amplitude and phase, $\tilde{A}(s, \varepsilon)\exp(\mathrm{i}\phi(s)/\varepsilon)$, that will enable the matching process to proceed in the subsequent development of the solution. To determine C in the Fourier transformed domain, we transform the inner boundary

condition using equation (17),

$$g(k, \varepsilon) = \frac{1}{2\pi} \int_{-\infty}^{\infty} \tilde{A}(s, \varepsilon)\, \mathrm{e}^{\mathrm{i}\phi(s)/\varepsilon}\, \mathrm{e}^{-\mathrm{i}ks}\, \mathrm{d}s. \tag{20}$$

Hence, as $\bar{r} \to 0$, $\tilde{u} \to g(k, \varepsilon)$. Therefore,

$$\tilde{u} \sim g(k, \varepsilon) y^{a/2} \mathrm{H}_q^{(1)}(\mathrm{i}\xi y^{1/2}). \tag{21}$$

Finally, using the transformed equation that relates $\tilde{u}$ to $\tilde{p}$, we use the inverse Fourier transform to obtain the outer solution in the form

$$p^o(\bar{r}, s) = \int_{-\infty}^{\infty} g(k, \varepsilon) \left[1 + \mathrm{i}\, \frac{\varepsilon^3}{\omega - \varepsilon k \bar{u}_\infty} \frac{\bar{v}_\infty}{\bar{r}} \frac{\partial}{\partial \bar{r}} \right] \{ y^{a/2} \mathrm{H}_q^{(1)}(\mathrm{i}\xi y^{1/2}) \}\, \mathrm{e}^{\mathrm{i}ks}\, \mathrm{d}k. \tag{22}$$

2.4. MATCHING TO LOWEST ORDER

The inner solution results from asymptotically expanding the equations that apply to the inner region. As a consequence, it does not satisfy the outer boundary conditions of the problem that lie in the outer region. Conversely, the outer solution does not satisfy boundary conditions that are in the inner region. Each part of the problem has missing conditions that are satisfied by the process of matching the two solutions using the intermediate matching principle [26, 41]. The intermediate matching principle defines an intermediate variable and expands the inner and the outer solutions in terms of this variable. These two intermediate solutions must overlap in some domain whereby the difference between the inner and the outer solutions must vanish to the appropriate order in the intermediate limit.

The intermediate variable is defined as

$$\tilde{r} = r\varepsilon^{1/K}, \tag{23}$$

where K is a large positive number. In terms of the outer variable $\bar{r}$, we obtain

$$\bar{r} = \varepsilon r = \tilde{r}\varepsilon^{1 - 1/K}. \tag{24}$$

This substitution is used in equation (22) to transform from the $(\bar{r}, s)$ co-ordinates to the $(\tilde{r}, s)$ co-ordinates. The resulting equation is then asymptotically evaluated as $\varepsilon \to 0$, keeping $\tilde{r}$ fixed. This is the intermediate limit. To accomplish this evaluation, we first let $\eta = \varepsilon k$ in equation (20) and use the saddle point method to obtain an asymptotic solution for $g(\eta/\varepsilon, \varepsilon)$. This result is substituted into equation (22) and again, after letting $\eta = \varepsilon k$, the integral is asymptotically evaluated by using the saddle point method. This method is described in both Bender and Orszag [42] and Dingle [43], with further details specific to this evaluation given in Dahl [37]. After much algebraic manipulation, the intermediate limit to lowest order for the outer solution is given by

$$p^o(\tilde{r}, s) \sim \mathrm{e}^{\mathrm{i}\phi(s)/\varepsilon} \overline{A}_0(s) \mathrm{H}_n^{(1)}(\mathrm{i}\lambda(\alpha)\varepsilon^{-1/K}\tilde{r}) + O(\varepsilon \ln \varepsilon). \tag{25}$$

We now want to match the outer solution expansion to the inner solution expansion in the intermediate co-ordinates. Using the lowest order form of equation (10), with $\hat{p}_0(\bar{r}, s)$ represented by equation (16), we first replace the radial co-ordinate by the intermediate transformation $r = \tilde{r}\varepsilon^{-1/K}$. Next, the intermediate limit for the inner expansion is found by letting $\varepsilon \to 0$ with $\tilde{r}$ fixed. This results in the intermediate radial parameter in the general functions in equation (16) becoming large. Since for a large radial argument equation (16) approaches equation (13), then in the intermediate limit $\zeta_1^p \to \mathrm{H}_n^{(1)}$

and $\zeta_2^p \to H_n^{(2)}$. Thus,

$$p_0^i(\tilde{r}, s) \sim e^{i\phi(s)/\varepsilon}[A_0(s)H_n^{(1)}(i\lambda(\alpha)\varepsilon^{-1/K}\tilde{r}) + B_0(s)H_n^{(2)}(i\lambda(\alpha)\varepsilon^{-1/K}\tilde{r})] + O(\varepsilon \ln \varepsilon). \quad (26)$$

Comparing equation (26) with equation (25), we see that

$$A_0(s) = \tilde{A}_0(s), \qquad B_0(s) = 0. \quad (27, 28)$$

This result and the condition of finite value at $r = 0$ turns the $m = 0$ solution of equation (11) into an eigenvalue problem with solutions only for certain values of the eigenvalue α.

A complete solution of the problem to $O(1)$ may be found by analyzing the equations for the expansion terms $m = 1$ and $m = 2$ and performing the higher order matching process [26, 37]. The results would show the changes in $A_0(s)$ due to a slowly diverging jet mean flow. The effect of flow divergence on stability results from supersonic jets is small. Tam *et al*. [32] neglect this effect in calculating the instability waves in a Mach 2 hot jet. In an extension of the model to include a wide spectrum of frequencies. Tam and Chen [44] assume that the validity of the model would not be affected by neglecting the flow divergence. The same assumption is made for instability wave calculations in supersonic elliptic jets [45]. The instability wave characteristics are then governed by the local eigenvalues at each axial location, known as the locally parallel flow approximation. The growth and decay of the instability wave is then governed solely by the spreading of the mean flow and the effect of the change in the eigenfunction shape with axial distance is neglected. We will follow this assumption in our estimates of the instability wave characteristics in supersonic coaxial jets. Thus, the amplitude function in the lowest order form of equation (20) becomes a constant,

$$\tilde{A}_0(s) = \hat{A}_0, \quad (29)$$

and the phase term is found from

$$\phi(\varepsilon x)/\varepsilon = \int_0^x \alpha(\chi)\, d\chi. \quad (30)$$

2.5. NEAR FIELD PRESSURE

The near field pressure disturbances outside the jet are found from an asymptotic expansion of equation (22). To $O(1)$, the pressure disturbance equation, including the azimuthal and time dependencies, is

$$p'(r, \theta, x\, t) = \int_{-\infty}^{\infty} g(\eta)H_n^{(1)}(i\lambda(\eta)r)\, e^{i\eta x}\, e^{in\theta}\, e^{-i\omega t}\, d\eta, \quad (31)$$

where

$$g(\eta) = \frac{1}{2\pi}\int_{-\infty}^{\infty} \hat{A}_0\, e^{i\phi x(\varepsilon x)/\varepsilon}\, e^{-i\eta x}\, dx. \quad (32)$$

Equations (31) and (32) take the axial evolution of the nth mode spatial instability wave described by $\hat{A}_0 \exp(i\phi/\varepsilon)$, Fourier transform it into wavenumber space, multiply it by a "propagator" function $H_n^{(1)}$, and then inverse Fourier transform the result back to physical space. In essence, the instability wave is considered as the source in a radiation problem in which, in the near field, there are both propagating and non-propagating waves. It is the propagating waves that reach the far field as sound.

2.6. FAR FIELD PRESSURE

To obtain an estimate of the sound radiated to the far field, it is convenient to transform equation (31) from cylindrical to spherical co-ordinates using

$$x = R\cos\psi, \qquad r = R\sin\psi. \tag{33}$$

The resulting integral is evaluated for large R by the method of stationary phase [46]. The far field pressure is then used to determine the sound power radiated per unit solid angle [47],

$$D(\psi) = \tfrac{1}{2}|p'|^2R^2 = 2\,\frac{|g(\bar{\eta})|^2}{[1 - M_\infty^2\sin^2\psi]}, \tag{34}$$

where the stationary phase point $\bar{\eta}$ is given by

$$\bar{\eta} = \frac{\bar{\rho}_\infty^{1/2}M_1\omega\cos\psi}{(1 - M_\infty^2)(1 - M_\infty^2\sin^2\psi)^{1/2}} - \frac{\bar{\rho}_\infty M_1^2\bar{u}_\infty\omega}{1 - M_\infty^2} \tag{35}$$

and ψ is the polar angle.

To find the angular dependence of $g(\bar{\eta})$, equation (35) must be solved for ψ in terms of $\bar{\eta}$. When this is done, we find that solutions only exist for $\bar{\eta} < \bar{\eta}_c$, where

$$\bar{\eta}_c = \bar{\rho}_\infty^{1/2}M_1\omega/(1 + M_\infty), \tag{36}$$

limiting ψ such that $0 \leqslant \psi \leqslant \pi/2$.

2.7. NUMERICAL FORMULATION

Equation (11) must be solved numerically to obtain results for various flow conditions in a supersonic coaxial jet.

2.7.1. *Eigenvalue problem*

Finite differencing equation (11) for $m = 0$ is one of the alternatives for obtaining a numerical solution to the eigenvalue problem [48, 49]. It is easily applied using the same evenly spaced r-grid on which the mean flow was calculated and it provides a simple means to determine an initial guess for the eigenvalue. We rewrite equation (11) as

$$\frac{\partial^2\hat{p}_0}{\partial r^2} + \left[\frac{1}{r} + \frac{2}{c - \bar{u}}\frac{\partial\bar{u}}{\partial r} - \frac{1}{\bar{\rho}}\frac{\partial\bar{\rho}}{\partial r}\right]\frac{\partial\hat{p}_0}{\partial r} + \left[\bar{\rho}M_1^2\left(\frac{\omega}{c}\right)^2(c - \bar{u})^2 - \frac{n^2}{r^2} - \left(\frac{\omega}{c}\right)^2\right]\hat{p}_0 = 0, \tag{37}$$

where $c = \omega/\alpha$. For the spatial stability problem, ω is real and c is complex, $c = c_r + \mathrm{i}c_i$ (as is $\alpha = \alpha_r + \mathrm{i}\alpha_i$). Changing the eigenvalue from α to c confines the range in which the eigenvalue lies in the complex c-plane. Given any real ω, the eigenvalue c will have a real part, c_r, that is within or near the bounds set by the real mean velocity $\bar{u}$. Thus, c is easily found compared to α and the numerical technique is more easily controlled, since c lies within a limited range. Furthermore, in the initial region of a coaxial jet with two thin shear layers and two eigenvalues, using c as the eigenvalue allows easy identification of which c belongs to which shear layer.

For eigenvalues representing growing waves, we apply central differencing to the derivatives in equation (37) and rearrange into tridiagonal form to obtain the following

difference equation

$$[1 - \tfrac{1}{2}Z_{1k}\Delta r]\,\hat{p}_{k-1} + [Z_{0k}\Delta r^2 - 2]\,\hat{p}_k + [1 + \tfrac{1}{2}Z_{1k}\Delta r]\,\hat{p}_{k+1} = 0, \tag{38}$$

where

$$Z_{1k} = \left[\frac{1}{r} + \frac{2}{c - \bar{u}}\frac{\partial \bar{u}}{\partial r} - \frac{1}{\bar{\rho}}\frac{\partial \bar{\rho}}{\partial r}\right]_k$$

and

$$Z_{0k} = [\bar{\rho}M_1^2(\omega/c)^2(c - \bar{u})^2 - n^2/r^2 - (\omega/c)^2]_k$$

are known at each interior grid point $k = 2, 3, \ldots, N$.

2.7.2. *Boundary conditions*

The inner boundary condition for equation (37) depends on whether the eigenfunction is axisymmetric, $n = 0$, or non-axisymmetric, $n \neq 0$. Axisymmetry requires that the eigenfunction have a zero first derivative on the axis. For non-axisymmetry, the eigenfunction has opposite signs either side of the axis, hence, the eigenfunction must be zero on the axis. In equation form, the inner boundary conditions at $k = 1$ are written as

$$\frac{\partial \hat{p}_1}{\partial r} = 0, \qquad n = 0; \qquad \hat{p}_1 = 0, \qquad n \neq 0. \tag{39}$$

The outer boundary condition was defined by equation (13) and from matching $B_0 = 0$. Taking the ratio of the two outermost grid points to eliminate A_0, we rearrange the results to obtain

$$-\frac{\mathrm{H}_n^{(1)}(\mathrm{i}\lambda r_{N+1})}{\mathrm{H}_n^{(1)}(\mathrm{i}\lambda r_N)}\,\hat{p}_N + \hat{p}_{N+1} = 0 \tag{40}$$

for the outer boundary condition.

2.7.3 *Methodology of numerical solution*

Equations (38), (39) and (40) create a tridiagonal system of equations that can be written as

$$\mathbf{A}(c)\mathbf{p} = 0. \tag{41}$$

This equation forms a generalized eigenvalue problem [50] which has a non-trivial solution only when

$$\det[\mathbf{A}(c)] = 0. \tag{42}$$

The determinant of $\mathbf{A}$ is easily calculated as the product of the diagonal terms in an LU-decomposition of $\mathbf{A}$.

The solution of equation (42) requires an initial guess for the eigenvalue c. The form of this equation provides an easy means of finding an initial guess. For a complex c, the determinant of $\mathbf{A}$ is, in general, also complex. Setting up a grid over the region in which the eigenvalue is suspected to lie, the determinant of $\mathbf{A}$ is calculated at each point. Contours are then drawn through the region that define the zeroes of the real part and the imaginary part of $\det[\mathbf{A}(c)]$. These contours only cross at the eigenvalue. Once the initial guess for the eigenvalue is made, refinement of its value is achieved using the Newton–Raphson iteration method.

For a typical instability wave calculation, the eigenvalue must be found at every axial location for a given frequency ω. The contour grid method is performed at the first

upstream profile. Thereafter, the eigenvalue solution at the previous axial location can be used as the initial guess for the eigenvalue at the next axial location. Extrapolating the first guessed eigenvalue at the next axial location from previous values often speeds up the convergence, as long as the mean flow profiles are slowly changing.

2.7.4. *Contour solution*

The numerical solution set out above has been discussed in terms of growing eigenvalues where $c_i > 0$. Implicit in the discussion was that the solution can then be calculated along the real r-axis. However, in order to continue the inviscid stability calculations into the damped region, $c_i < 0$, it is well known that a contour deformation must be made into the complex r-plane to avoid the critical point, r_c, at which $c - \bar{u}(r_c) = 0$ [26, 40, 51, 52]. If all of the variables in equation (37) are assumed to be analytic, then any contour can be chosen that avoids the critical point [53]. In our case, however, $\bar{u}$ and $\bar{\rho}$ are only known on the real axis. To obtain their values in the complex plane, a Taylor series expansion is taken about the real axis. This analytic continuation into the complex plane was found to be simpler to calculate along a simple box path around r_c rather than using complex mapping.

The direction of the contour into the complex r-plane is determined from the derivative of the mean velocity profile. For normal profile jets, $\partial\bar{u}/\partial r \leqslant 0$. The critical point for a growing mode lies in the lower half-plane and passes into the upper half-plane when damped. The contour for damped waves must then go into the upper half-plane to go around the critical point, since the branch cut associated with the critical point goes to $-\infty$ in the direction of the negative imaginary axis. The reverse is true for the inverted profile jet where, in the inner shear layer, $\partial\bar{u}/\partial r > 0$. The contour must go below the damped critical point in the lower half-plane as the branch cut goes to $+\infty$.

Once the numerical differencing along the contour was completed, the system of equations was found to be augmented by the number of grid points that were added along the vertical parts of one or two box contours [37]. The formalism of the solution as previously described did not change as the calculations proceeded from the growing to the damped eigenvalue solutions.

2.7.5. *Near and far field pressures*

Both the near field pressure solution, equation (31), and the far field pressure directivity, equation (34), depend upon the Fourier transform of the instability wave; equation (32). We can use the fast Fourier transform (FFT) to perform the calculations [54]. Using the trapezoidal rule, equation (30) is written as

$$\phi_j = \phi_{j-1} + \tfrac{1}{2}(\alpha_j + \alpha_{j-1})(x_j - x_{j-1}), \tag{43}$$

where $\phi_0 = 0$ and $j = 1, 2, \ldots, J$.

Setting $\hat{A}_0 = 1$, the discrete Fourier transform of the instability wave becomes

$$\{\exp(\mathrm{i}\phi_j)\}_m = \sum_{j=0}^{M-1} \exp(\mathrm{i}\phi_j)\, \mathrm{e}^{-\mathrm{i}2\pi mj/M}, \tag{44}$$

where, by definition for $j > J$, $\exp(\mathrm{i}\phi_j) = 0$. With $M > J$, we have zero padded the FFT of the instability wave and increased the resolution in the wavenumber spectrum,

since

$$\Delta\eta = 2\pi/M\Delta x. \tag{45}$$

Finally, the wavenumber spectrum of the instability wave is given by

$$g(\eta_m) = \frac{\Delta x}{2\pi}\{\exp(\mathrm{i}\phi_j)\}_m, \tag{46}$$

where

$$\eta_m = \begin{cases} m\Delta\eta, & 0 \leqslant m \leqslant M/2 - 1, \\ (m - M)\Delta\eta, & M/2 \leqslant m \leqslant M - 1. \end{cases} \tag{47}$$

The first half of the FFT contains the spectrum for positive wavenumbers and the second half contains the spectrum for the negative wavenumbers.

To solve for the near field pressure, we recognize that equation (31) has the form of a convolution integral that is being solved in the transform domain. A formulation has been devised for correctly solving a two-dimensional form of this equation in which the propagator function, in our case $\mathrm{H}_n^{(1)}$, is known analytically [55, 56]. The formulation is easily written for our one-dimensional problem where (ignoring the θ and t dependences) equation (31) becomes

$$p'(r, x_j) = \{\{\exp(\mathrm{i}\phi_j)\}_m \mathrm{H}_n^{(1)}(\mathrm{i}\lambda(\eta_m)r)\}_j \tag{48}$$

and the inverse discrete Fourier transform is defined by

$$\{f_m\}_j = \frac{1}{M}\sum_{m=0}^{M-1} f_m \, \mathrm{e}^{\mathrm{i}2\pi mj/M}, \tag{49}$$

η_m is defined in equation (47). To reduce errors, the zero padding in equation (44) must have $M \geqslant 2J$. Further possible errors are minimized by replacing $\mathrm{H}_n^{(1)}$ in equation (48) by an integrated average over the wavenumber resolution $\Delta\eta$ at each η_m [56].

The far field directivity is determined directly by substitution of equation (46) into equation (34) and using only positive wavenumbers. For each η_m, the angular dependence ψ is determined from the inverse of equation (35) up to the limit set by equation (36).

2.7.6. *Numerical accuracy*

The system of equations represented by equation (41) is second order accurate on the real axis for the numerical differencing of the disturbance pressure. However, the mean flow quantities, as shown in Part 1 of this paper [31], are found from a first order accurate numerical scheme. This formally reduces the accuracy of the numerical eigenvalue problem to the first order dependent on the r-grid spacing used in the mean flow calculations. The effect of grid spacing on the eigenvalue calculations is shown in Figure 3 for a compressible jet. (Mean flow spreading parameters are shown in Figure 5 of Part 1). For the initially thin axisymmetric shear layer, the growth rate and phase velocity for the first helical mode at $fD_1/U_1 = 0{\cdot}2$ where D_1 is the jet exit diameter, are underestimated if the grid resolution is insufficient. As the flow expands downstream and the shear layer becomes larger, the eigenvalue results converge to the same value. The ability to calculate the correct eigenvalue is primarily dependent on accurate values for the first derivatives of the mean flow quantities. For the initial thin shear layer, the edges of the shear layer are sharp, with rapid changes in the derivative values. With a course grid, these values are inaccurately represented. As the flow smooths out, the derivatives change more gradually and the numerical representation for the derivatives is more accurately obtained with the course

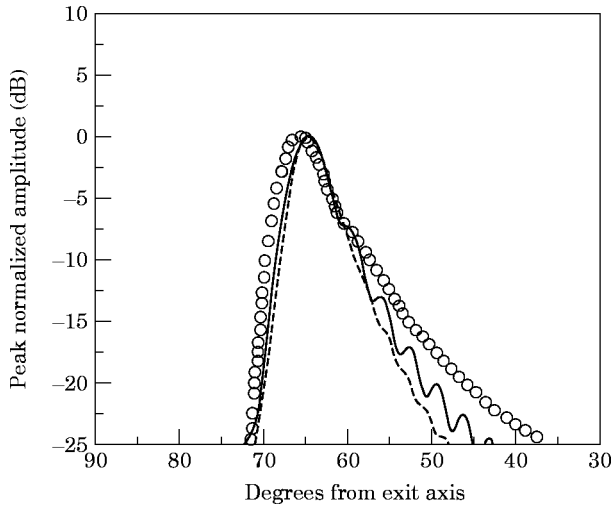

Figure 5. A comparison of results from the far field directivity calculations for a single jet: $n = 1, fD_1/U_1 = 0{\cdot}4$. See Figure 4 for legend.

grid. Thus, a fine grid is initially required to obtain accurate representation of the mean flow derivatives at the edges of the thin shear layer.

2.8. COMPARISONS WITH ANALYTIC STUDIES

The numerical procedures described in this paper, and in Part 1 [31], are designed to use the jet exit operating conditions as the only known inputs into calculating the local stability characteristics and the far field directivity patterns of axisymmetric jets with both single and dual systems. This allows a wider variety of operating conditions to be studied

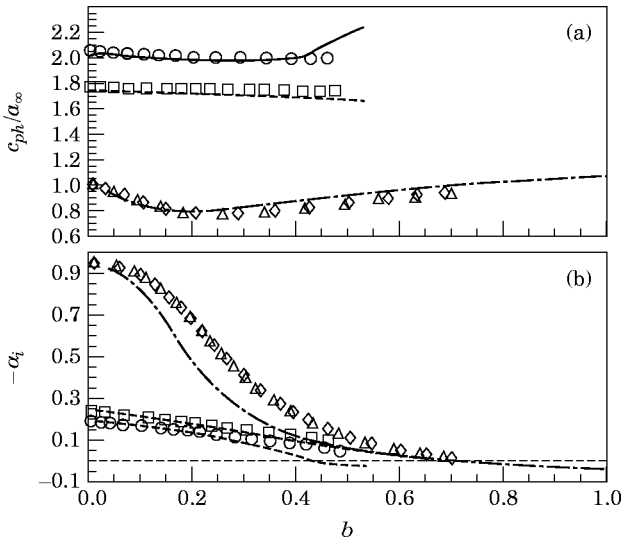

Figure 6. The stability characteristics for a NVP coaxial jet as a function of local shear layer half-width b: $fD_1/U_1 = 0{\cdot}2$. Calculated results using numerically generated mean flow: inner shear layer, ———, $n=0$; ----, $n = 1$; outer shear layer, — — —, $n = 0$; — - — -, $n = 1$. Results from reference [23] mean flow defined by analytic functions: inner shear layer, ○, $n = 0$; □, $n = 1$; outer shear layer, ◇, $n = 0$; △, $n = 1$. (a) Phase velocity relative to ambient speed of sound; (b) growth rate.

TABLE 1

Operating conditions for the supersonic coaxial jet calculations

AR	*r*	*s*	U_1 (m/s)	U_2 (m/s)	T_1 (K)	T_2 (K)	M_1	M_2
Reference jet								
—	—	—	1330·0	—	1100·0	—	2·0	—
NVP jets								
1·25	0·80	1·00	1477·8	1182·2	1086·4	1086·4	2·2	1·8
1·25	0·60	1·00	1605·2	963·1	1032·6	1032·6	2·5	1·5
1·25	0·40	1·00	1662·2	665·0	916·7	916·7	2·7	1·1
1·25	0·20	1·00	1583·3	316·7	727·5	727·5	2·9	0·6
1·25	0·80	2·00	1534·6	1227·7	1692·3	846·2	1·9	2·1
1·25	0·60	2·00	1750·0	1050·0	1608·2	804·1	2·2	1·8
1·25	0·40	2·00	1900·0	760·0	1396·8	698·4	2·5	1·4
1·25	0·80	0·50	1425·0	1140·0	785·7	1571·4	2·5	1·4
1·25	0·60	0·50	1492·8	895·7	754·5	1509·1	2·7	1·2
1·25	0·40	0·50	1511·4	604·5	694·4	1388·9	2·9	0·8
1·00	0·80	2·00	1516·7	1213·3	1630·7	815·3	1·9	2·1
0·75	0·80	2·00	1492·8	1194·3	1552·2	776·1	1·9	2·1
0·50	0·80	2·00	1459·7	1167·8	1448·8	724·4	1·9	2·2
1·00	0·40	2·00	1813·6	725·5	1350·0	675·0	2·5	1·4
0·75	0·40	2·00	1716·1	686·5	1297·7	648·8	2·4	1·3
0·50	0·40	2·00	1605·2	642·1	1239·1	619·5	2·3	1·3

Area ratio $AR = A_2/A_1$; velocity ratio $r = U_2/U_1$; density ratio $s = \rho_2/\rho_1 = T_1/T_2$, (constant thrust and constant mass flow).

without relying on measured mean flow parameters, especially in the case of supersonic coaxial jets, for which mean flow data are hard to obtain. To validate our procedures, we chose both single axisymmetric jet and coaxial jet cases, in which both the mean flow was defined and the stability calculations had been completed under supersonic conditions. The results from our stability calculations have been compared with the results from these reference cases, in which the mean flow was represented by analytic functions for the axial velocity and by Crocco's relation for the density, an approach typically used in past studies of jet stability characteristics. For the far field directivity patterns, our calculated results are compared with results from calculations using analytic functions to describe single axisymmetric jet mean flows.

A single, hot, Mach 2, perfectly expanded jet was defined by measurements taken by Seiner *et al*. [57]. The measured jet parameters included the centerline velocity, the radius to the half-velocity point, and the half-width of the mixing layer, all as functions of axial distance. These parameters were used to define the mean flow velocity by a half-Gaussian analytic function, which was then used in the stability calculations [33]. Example results from these calculations for a single jet with a static temperature of 761 K are shown in Figure 4 for the first helical mode ($n = 1$) at a Strouhal number of 0·4 (open symbols). Two comparisons are made with this analytic data using the numerical mean flow. The first set of results use the mean flow generated with the turbulence model as defined in Part 1 of this paper [31]. This mean flow overestimated the potential core length by 37% and had a lower spreading rate compared to measured data. Nonetheless, our calculations give similarly shaped growth rate and phase velocity curves (dashed lines in Figure 4). In the second set of results, the mean flow calculations are modified to match the potential core length of the measured mean flow data. This is done by increasing the coefficient in the turbulence mode [58]. The stability calculations result in growth rates and phase velocities that are in better agreement with the analytical calculations. The discrepancies

are now due to an inexact match for the shear layer spreading rate and differences in profile shaping. The latter has been shown to cause differences in stability calculations [59].

The corresponding far field directivity patterns for these single jet stability calculations are shown in Figure 5. These results show the relative insensitivity of the peak direction in the far field directivity pattern to moderate changes in the mean flow profile shape and the jet shear layer spreading rate. Thus, we have shown that the numerically generated mean flow can provide reasonable input profiles for calculating stability and noise results that compare favorably with results from analytical calculations based on measured jet parameters for single axisymetric jets. Furthermore, other jet operating conditions can be chosen in which no measured data exists in order to study the relative changes that occur in the stability and noise generation characteristics of a supersonic jet.

No set of mean flow measurements have been taken in a supersonic coaxial jet and used to create a set of axially varying parameters for analytic function descriptions of both the mean flow velocity and density at all axial locations. However, Bhat and Seiner [23] developed an analytic model for the initial mean flow of a supersonic coaxial jet for the purpose of conducting stability calculations. They modelled the two shear layers separately which enabled them to define the mean flow out to the end of the outer potential core. Due to a lack of measured data, they recognized that they could not continue the analytic function flow modelling into the merging and fully developed flow regions downstream. The mean velocity profiles were defined by half-Gaussian functions and the spreading rates were determined from the Langley curve. Crocco's relation was used to define the mean density profiles. For the stability calculations, the Rayleigh equation was integrated numerically across each shear layer separately, using analytic functions in the regions of constant mean flow properties to define the four boundary conditions. These calculations resulted in local growth rates and phase velocities as a function of axial distance. An example of their results is shown in Figure 6 for an NVP jet with the following operating conditions: $R_2/R_1 = 3{\cdot}0$, $M_1 = M_2 = 1{\cdot}48$, $U_2/U_1 = 0{\cdot}52$, $T_2/T_1 = 0{\cdot}27$, $T_\infty/T_1 = 0{\cdot}37$. Both axisymmetric ($n = 0$) and first helical ($n = 1$) modes are shown for a Strouhal number of $fD_1/U_1 = 0{\cdot}2$. The results are plotted against the local shear layer half-width appropriate to the shear layer with which the eigenvalue is identified; either the inner or outer shear layer. For comparison, the results from our stability calculations are shown in the same figure. Given that no attempt was made to match the spreading rate in the numerical mean flow model to the spreading rates used for the analytic function profiles, the numerical results are very similar to the analytic results when plotted versus the local shear layer half-width. Where the shear layers are thin, the growth rates and phase velocities are almost identical. The primary differences that occur downstream can be attributed to the differences in profile shaping.

The results shown in Figure 6 for a NVP jet validate our procedure for stability calculations in coaxial jets. The reference analytic function calculations seek to find the eigenvalues in each shear layer by integrating the Rayleigh equation across each layer separately and coupling the integrations through the boundary condition in the outer potential core; whereas we do not use an intermediate boundary condition, but integrate across the total jet flow using only an outer free stream boundary condition and a symmetry boundary condition on the jet centerline. Thus, the effects of the presence of the two shear layers is directly coupled within the calculations.

3. NUMERICAL PREDICTIONS

The mean flow formulation from Part 1 of this paper [31] and the stability wave noise generation model from the previous section were used to study the effect of changing

various operating parameters on the instability wave noise generation from perfectly expanded, supersonic NVP coaxial jets. We chose the operating conditions to have the same total thrust, mass flow, and exit area as a single reference jet using the formulations given in Dahl [37]. The values chosen for the present study are shown in Table 1. The single reference jet had an exit velocity of 1330 m/s and an exit static temperature of 1100 K

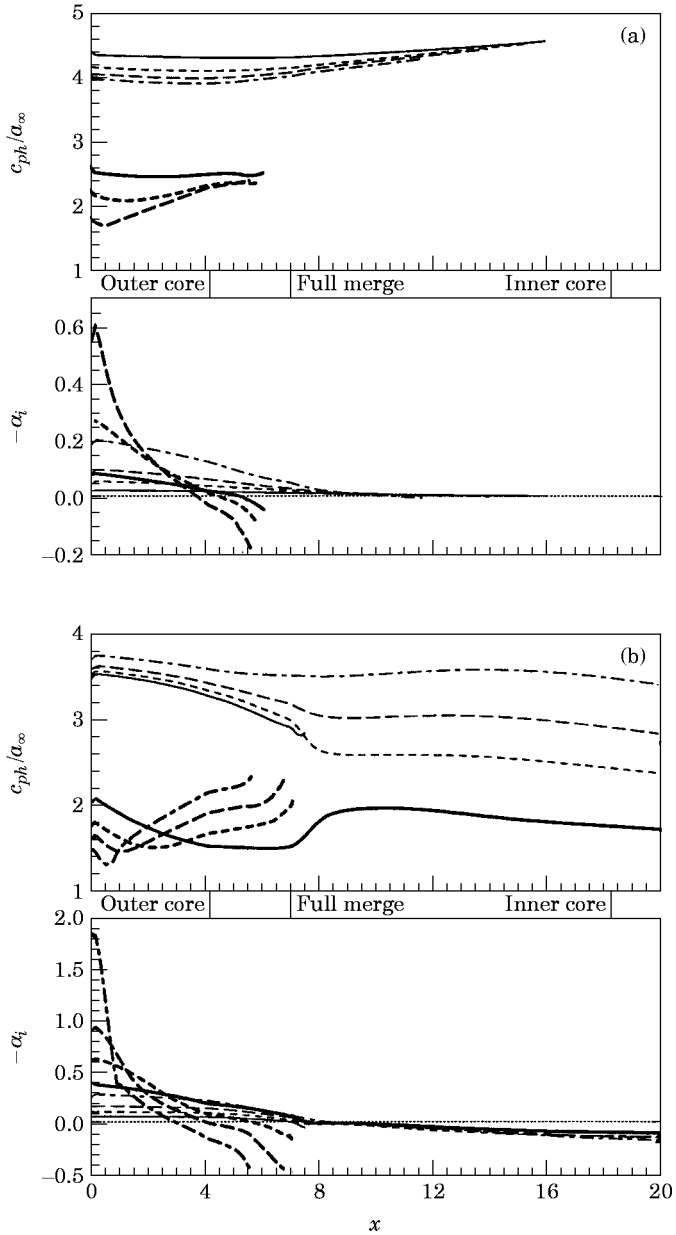

Figure 7. Growth rates and phase velocities relative to the ambient speed of sound for both shear layers of a NVP jet with $U_2/U_1 = 0{\cdot}6$, $\rho_2/\rho_1 = 1{\cdot}0$, and $AR = 1{\cdot}25$. The legend defines lines with numbered pairs (fD_e/U_e, maximum amplitude from equation (50)). (a) $n = 0$, inner shear layer: ———, 0·06, 1·162; ----, 0·12, 1·358; — — —, 0·20, 1·632; — - — -, 0·40, 2·583. Outer shear layer: ———, 0·06, 1·252; - - - -, 0·12, 1·710; — — —, 0·20, 2·126. (b) $n = 1$, inner shear layer: ———, 0·06, 1·320; ----, 0·12, 1·731; — — —, 0·20, 2·380; — - — -, 0·40, 4·170. Outer shear layer: ———, 0·06, 4·711; - - - -, 0·12, 4·585; — — —, 0·20, 4·207; — - — -, 0·40, 4·124.

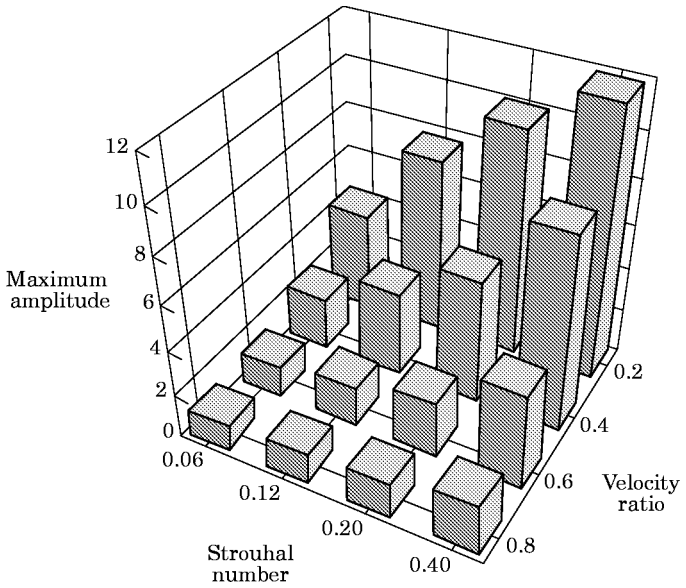

Figure 8. The effects of the velocity ratio and the Strouhal number on the maximum amplitude of instability waves in the inner shear layer: $n = 1$, $\rho_2/\rho_1 = 1{\cdot}0$, $AR = 1{\cdot}25$.

resulting in an exit Mach number of 2. When scaled up, this jet would produce thrusts and mass flows comparable to those projected for supersonic jet transport aircraft engines.

3.1. STABILITY CHARACTERISTICS

The mean flow prediction scheme was used to determine the development of the mean velocity and density profiles. These profiles were used to solve for the eigenvalues of the Rayleigh equation at every axial location. The real and imaginary parts of the eigenvalue may be identified with the local phase velocity and growth rate of the instability wave. Typical calculated values are shown in Figure 7 for an NVP jet, where part (a) contains results for the axisymmetric ($n = 0$) mode and part (b) contains results for the first helical ($n = 1$) mode. The NVP jet had a velocity ratio of $U_2/U_1 = 0{\cdot}6$ (indicating that the outer shear layer was larger in ΔU than the inner shear layer), a density ratio of $\rho_2/\rho_1 = 1{\cdot}0$, and an area ratio $AR = 1{\cdot}25$. The calculations were performed at four Strouhal numbers fD_e/U_e, where U_e and D_e are the exit velocity and diameter, respectively, of the reference jet and f is the cyclical frequency. This means that the calculations for each shear layer were performed at the same frequency. In the figure are indicated the axial location of the end of the outer potential core (where the two shear layers begin to merge), the axial location at which the two shear layers completely merge into a single shear layer, and the axial location of the end of the inner potential core. Also, an indication is given in the figure of the shear layer with which the stability characteristic is initially associated (inner and outer) and the maximum amplitude that the instability wave achieves relative to its initial amplitude. All of the stability characteristics shown are of the Kelvin–Helmholtz type. At Strouhal number 0·40, no Kelvin–Helmholtz type instability is found for the outer shear layer in the case of the $n = 0$ mode. All of the phase velocities shown are supersonic relative to the ambient speed of sound.

For the inner shear layer $n = 0$ mode, shown in Figure 7(a), stability calculations are continued downstream as far as possible until the phase velocity approaches the inner core velocity. After this point, no stability solutions are found. As the Strouhal number

increases, the inner shear layer growth rates increase while the phase velocities decrease. The instability wave continues to grow beyond the end of the outer potential core and slightly beyond the end of the merge region, but they are starting to damp soon after the merging of the shear layers.

The outer shear layer $n = 0$ mode stability characteristics are also shown in Figure 7(a). The initial growth rates also increase with Strouhal number and are larger than the comparable inner shear layer growth rates, but these growth rates decay more quickly than the inner shear layer growth rates. The outer shear layer phase velocities are lower than the inner shear layer phase velocities due to lower mean flow velocities, but they also decrease with increasing Strouhal number as do the inner shear layer phase velocities. These calculations are conducted until the phase velocity approaches the mean flow velocity at the point where the two shear layers are merging. As this happens, the damping rates start to increase toward larger values. Then, in the stability calculations, the critical point typically goes beyond the region in which the mean flow values in the complex plane are accurately calculated by analytic continuation and the calculations are stopped.

It is shown in Figure 7(b) that the initial growth rates in the inner shear layer for the $n = 1$ mode increase with Strouhal number. Unlike the $n = 0$ mode, these instability waves begin to damp at or soon after the end of the merge region. The phase velocities gradually increase with Strouhal number.

For the outer shear layer, the $n = 1$ mode growth rates shown in the figure initially increase with Strouhal number and are much larger than the inner shear layer growth rates. However, like the $n = 0$ mode, these growth rates decay more quickly than the inner shear layer growth rates, except for the Strouhal number 0·06 growth rates.

For the normal profile coaxial jet, the question arises of what happens to the two initially growing instability waves as the streams merge downstream into a single fully developed jet. This single jet would only have one $n = 1$ mode inviscid damped solution. Typical results from the stability calculations for a normal velocity profile jet are shown in Figure 7(b). With two shear layers, each having an initially growing instability wave, only

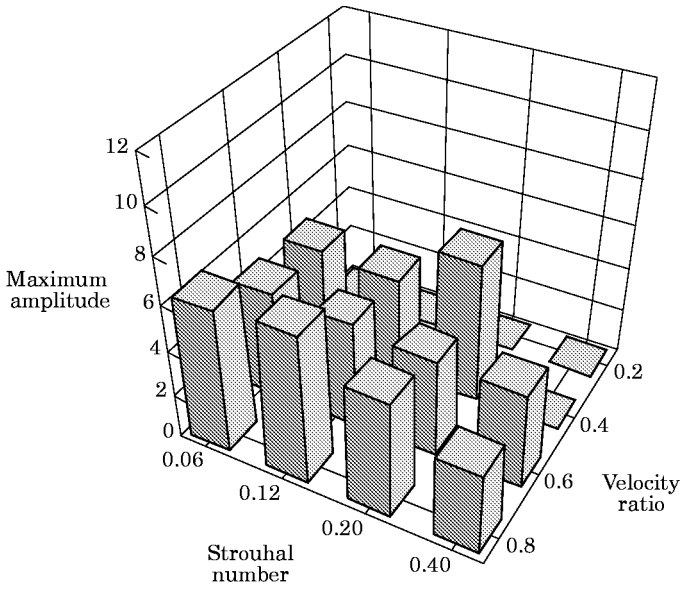

Figure 9. The effects of the velocity ratio and the Strouhal number on the maximum amplitude of instability waves in the outer shear layer: $n = 1$, $\rho_2/\rho_1 = 1{\cdot}0$, $AR = 1{\cdot}25$.

one of the two has a continuous solution into the downstream damped region of the single fully developed jet. The shear layer with the larger ΔU supports the lower Strouhal number waves that are continuous into the damped region and the shear layer with the smaller ΔU supports the higher Strouhal number waves. As can be seen, if the instability wave characteristics are continuous into the damped region in one shear layer, it is not continuous into the damped region in the other shear layer. The non-continuous instability wave characteristics become highly damped in the same manner as seen for the $n = 0$ mode. Again, in the stability calculations, the critical point goes beyond the path along which accurate mean flow calculations by analytic continuation are available. The concept of two eigenvalues merging is suggested by the behavior of the phase velocities. The inner shear layer phase velocities in Figure 7(b) decrease to the single jet phase velocity as the solution progresses downstream. In the outer shear layer, the phase velocities increase to the single jet phase velocity. No indication is found in the continuous damped eigenvalue solution that any other damped solution is nearby to suggest that the two solutions merge as the mean flow becomes fully developed.

The growth rate and phase velocity results in Figure 7 are typical for all of the normal velocity profile results. There are differences in the growth rate curves, especially, due to varying velocity and temperature ratios between the two streams. However, to judge the effects of operating condition changes, we will concentrate on comparing changes in the maximum amplitude obtained by the instability wave as a relative indication of the strength of the wave. The maximum amplitude is calculated by

$$A_{max} = \left| \exp \int_0^{x_c} \alpha(\chi)\, \mathrm{d}\chi \right|, \tag{50}$$

where x_c is the point at which $\alpha_i = 0$. In Figure 7, we note that the maximum amplitudes for the $n = 1$ modes are always larger than the maximum amplitudes for the $n = 0$ modes. Since for noise purposes we are interested in reducing the largest levels, in the remaining examples, we will only present the $n = 1$ results.

3.2. EFFECTS OF VELOCITY RATIO

To study the effects of velocity ratio in an NVP jet, the area ratio is fixed at 1·25 and the density ratio is fixed at 1·0. This results in a decrease in the static temperature of both streams as the velocity ratio decreases, as shown in Table 1, when the total thrust, mass flow and exit area are held constant. As the velocity ratio decreases from 0·8 to 0·2, the inner stream first increases in velocity and then begins to decrease before the velocity ratio equals 0·2 and the outer stream decreases in velocity. The Mach numbers increase continually for the inner stream and decrease for the outer stream. The effects of these changes on the growth of the first helical mode instability waves in both the inner and outer shear layers at four different Strouhal numbers are shown in Figures 8 and 9 in terms of the maximum amplitude of the instability waves calculated from equation (50). In both figures, the results are for Kelvin–Helmholtz type instability waves with supersonic phase velocities relative to ambient. The amplitude is set to zero in the figures if no wave of this type was found in the shear layer for the given operating conditions and Strouhal number. For example in Figure 9, the velocity ratio 0·2 case has a subsonic outer flow; hence, the instability waves have subsonic phase velocities.

In Figure 8 is shown the maximum amplitude of the instability waves in the inner shear layer as a function of the velocity ratio and the Strouhal number. These results follow the trend described by Michalke and Hermann [60] for an axisymmetric jet with an external flow. As the outer flow increases relative to the inner flow, that is, as the velocity ratio

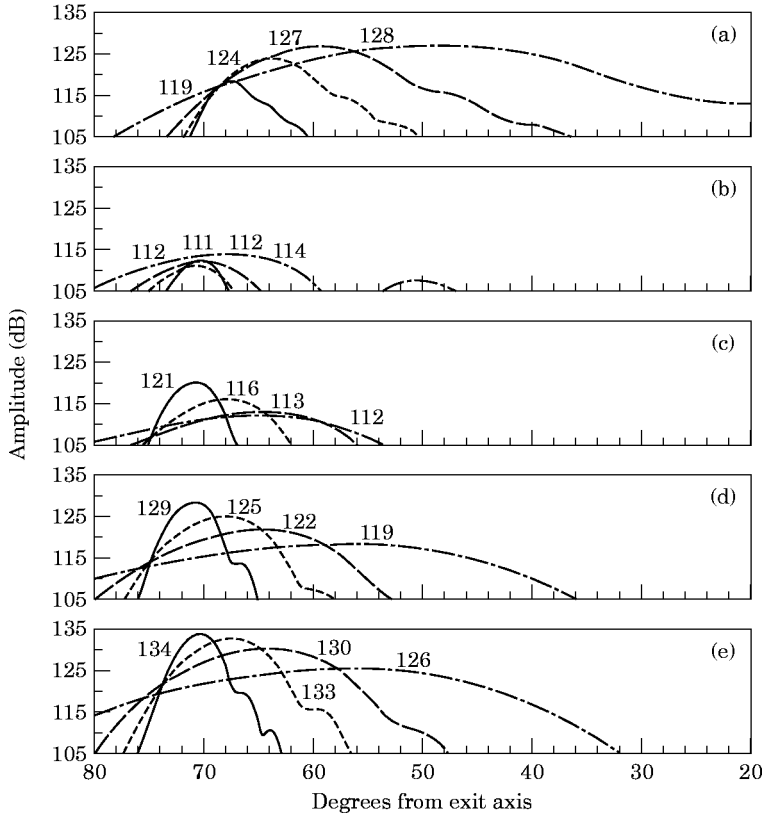

Figure 10. The effects of the velocity on the far field directivity patterns for noise radiated from instability waves in the inner shear layer. Numbers indicate peak amplitudes; $n = 1$, $\rho_2/\rho_1 = 1{\cdot}0$, $AR = 1{\cdot}25$. (a) Reference jet. NVP jet with $U_2/U_1 =$ (b) 0·8, (c) 0·6, (d) 0·4 (e) 0·2. Strouhal number: — - — -, 0·006; — — —, 0·12; ----, 0·20; ———, 0·40.

increases, the maximum instability wave amplitudes decrease. This occurs for all four Strouhal numbers shown in the figure. However, we note that for $U_2/U_1 < 0{\cdot}5$, where the inner shear layer has a larger ΔU than the outer shear layer, the instability waves continue to grow beyond the point at which the two shear layers merge into a single shear layer until they begin to decay before the end of the inner potential core. This allows the instability waves to grow to relatively large amplitudes. In contrast, when $U_2/U_1 > 0{\cdot}5$ and the inner shear layer has a smaller ΔU than the outer shear layer, the instability waves stop growing and begin to decay in the region in which the two shear layers merge into a single shear layer. Thus, the instability wave in the inner shear layer is not only affected by the outer jet flow, but it is also affected by the presence of the outer shear layer.

When the outer shear layer is larger than the inner shear layer, $U_2/U_1 > 0{\cdot}5$, the instability waves in the outer shear typically grow to greater amplitudes than those instability waves in the inner shear layer; compare Figure 9 with Figure 8. However, the large outer shear layer instability waves do not have as great an amplitude as the larger growing instability waves in the inner shear layer. The outer shear layer spreads more rapidly than the comparable size inner shear layer, since the velocity ratio across the outer shear layer is always near zero, which results in the fastest spreading rate for a shear layer. As the velocity ratio increases, the spreading rate will decrease. Thus, the outer shear layer local growth rates reach zero sooner in the axial direction.

The far field directivity patterns associated with the sound radiated by these instability waves are shown in Figure 10 for the inner shear layer instability waves and in Figure 11 for the outer shear layer instability waves. In both figures, the far field directivity patterns for the reference jet instability waves are shown for comparison. In the calculations, the initial instability wave amplitudes are set to 1, indicating that the assumption is used that the instability waves are excited by white noise at the nozzle exit [44]. Thus, the relative levels between different Strouhal number peaks are an indication of the relative levels of noise radiated by the different growing and decaying instability waves in each shear layer. The far field radiated noise for the reference jet is set to an arbitrary level and all NVP jet results are referenced to the same level. This allows comparisons to be made of the relative changes in noise radiation that occur when operating conditions are changed.

As the instability waves grow in the inner shear layer as the velocity ratio decreases, the noise radiated to the far field grows as shown in Figure 10. The radiated noise could grow to be larger than that radiated from the reference jet. This is the same type of trend noted by Tanna [7] for subsonic NVP jets at constant thrust, mass flow and exit area conditions. We also note that the inner shear layer promotes the growth of and the noise radiated from the higher Strouhal number instability waves relative to the lower Strouhal number instablity waves when comparing the noise radiated from the inner shear layer for $U_2/U_1 \leqslant 0{\cdot}6$ with the noise radiated from the reference jet.

The far field directivity patterns associated with the outer shear layer instability waves are shown in Figure 11. For $U_2/U_1 = 0{\cdot}8$, the outer shear layer is still large enough so that

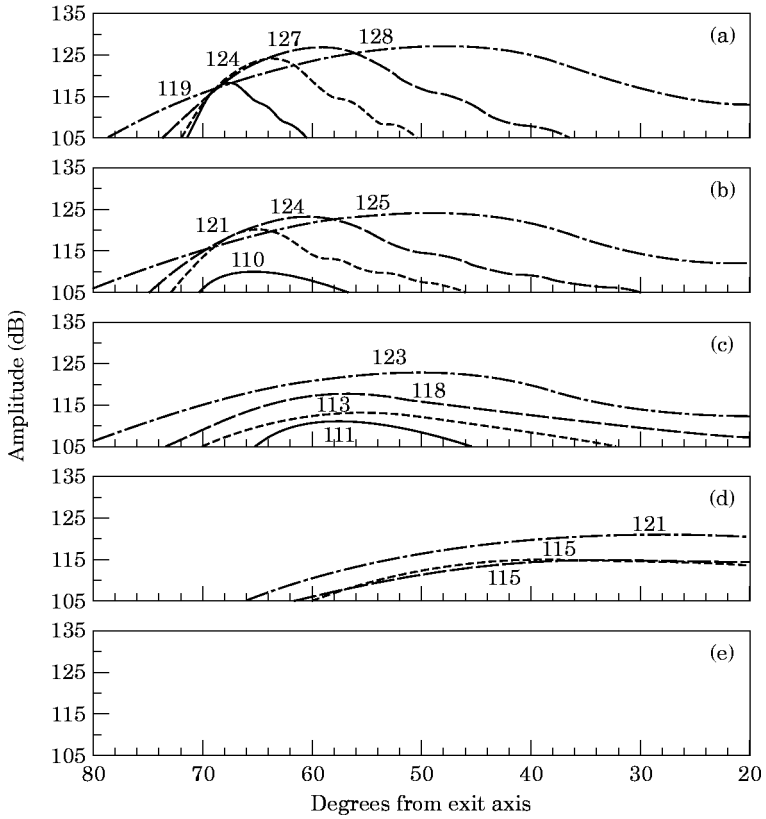

Figure 11. The effects of the velocity on the far field directivity patterns for noise radiated from instability waves in the outer shear layer. Numbers indicate peak amplitudes; $n = 1$, $\rho_2/\rho_1 = 1{\cdot}0$, $AR = 1{\cdot}25$. See Figure 10 for legend.

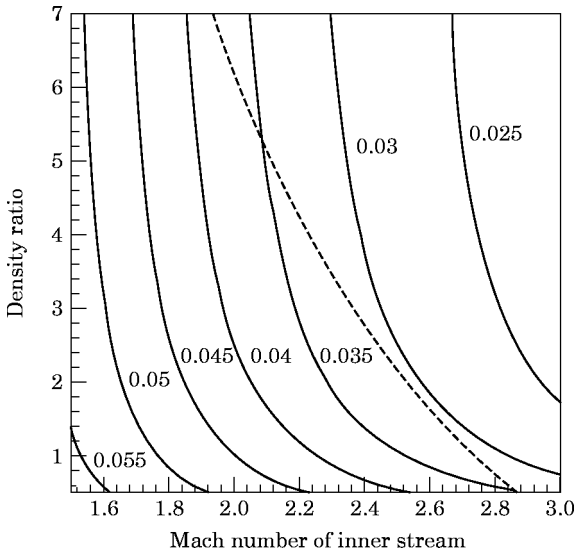

Figure 12. Contours of the constant compressible spreading rate, with a dashed line for the inner shear layer spreading rate of NVP jet with constant thrust, mass flow and exit area conditions: $U_2/U_1 = 0{\cdot}4$.

the relative levels of noise radiated from the lower Strouhal number instability waves are the same as that of the reference jet. However, due to the lower Mach number in the outer jet stream compared to the reference jet, the highest Strouhal number shows lower relative levels of radiated noise. As the velocity ratio continues to decrease, the Mach number decreases, causing the directivity peaks to shift toward zero degrees, the jet axis, as the phase speeds of in the instability waves decrease. At $U_2/U_1 = 0{\cdot}2$, the Mach number is subsonic and no instability wave components have supersonic phase speeds relative to

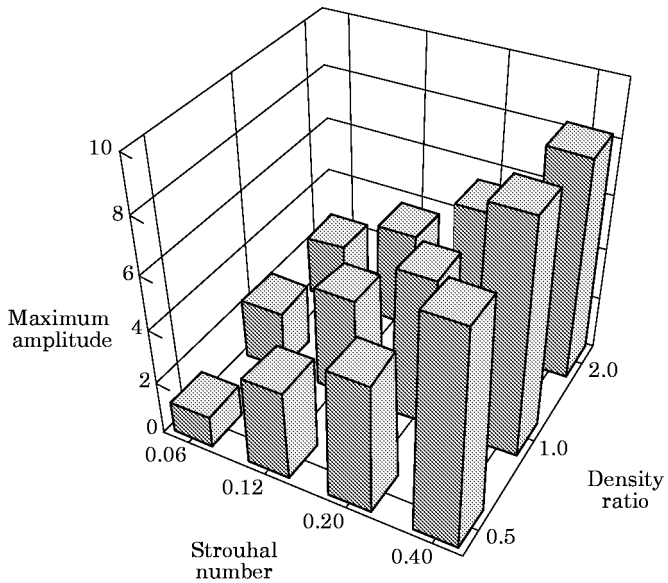

Figure 13. The effects of the density ratio and the Strouhal number on the maximum amplitude of instability waves in the inner shear layer: $n = 1$, $U_2/U_1 = 0{\cdot}4$, $AR = 1{\cdot}25$.

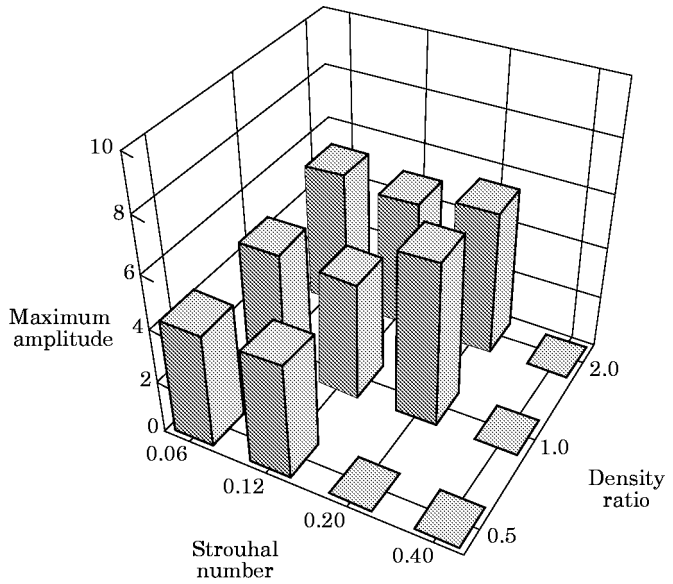

Figure 14. The effects of the density ratio and the Strouhal number on the maximum amplitude of instability waves in the outer shear layer: $n = 1$, $U_2/U_1 = 0{\cdot}4$, $AR = 1{\cdot}25$.

ambient. Thus, no noise radiates from the large scale structures at the chosen Strouhal numbers.

3.3. EFFECTS OF DENSITY RATIO

Many studies have been conducted about the effects of density ratio on the growth of instabilities and the spreading rates of planar and jet shear layers. Results for the normalized spreading rate show that this parameter decreases as the convective Mach number for the shear layer increases. In measurements of coaxial jets, Gutmark *et al*. [61] presented the measured compressible spreading rate non-normalized, as a function of velocity and density ratios. They concluded that, regardless of the convective Mach number, the compressible spreading rate and the level of instability increase for the inner shear layer as the velocity ratio decreases and as the density ratio increases. Our results for velocity ratio effects (Figure 8) agree with this conclusion. We will now consider the effects of density ratio in coaxial jets using two examples to illustrate our results.

In the first example, the velocity ratio between the outer and inner jet streams is fixed at 0·4; thus, the inner shear layer ΔU is larger than the outer shear layer ΔU. While maintaining the total thrust, mass flow and exit area constant and the area ratio set to 1·25, the density ratio is changed over three different values: 0·5, 1·0 and 2·0. The operating conditions are given in Table 1. Note that as the density ratio increases, the velocities in both streams decrease; however, due to the variations in temperatures, the Mach number increases for the inner stream and decreases for the outer stream. This set of operating conditions leads to the results that the initial spreading rate of the inner shear layer, based on the vorticity thickness, decreases from 0·0346 to 0·0311 as the density ratio is increased. This result tends to contradict the general remarks made by Gutmark *et al*. [61] because, as shown in Figure 12, the conclusion that one draws about the effects of density ratio on the compressible spreading rate depends on the path taken through the parameter space. The figure shows contours of compressible spreading rate δ'_ω, as defined from combining equations (A1), (A3) and (A4) in Part 1 of this paper [31], as a function of the

density ratio across the inner shear layer and the Mach number of the inner high speed stream. The dashed line is the path through the spreading rate space when the operating conditions are changed while maintaining a constant thrust, mass flow and exit area for the coaxial jet with $U_2/U_1 = 0{\cdot}4$. As can be seen, the compressible spreading rate along this path goes to a minimum at about a density ratio of 1·8. For the density ratio decreasing or increasing from this point, the compressible spreading rate increases. How this result affects the growing instability waves for $\rho_2/\rho_1 \leqslant 2$ is discussed next.

The maximum amplitudes of the growing $n = 1$ instability waves in the inner shear layer are shown in Figure 13 as a function of the density ratio and the Strouhal number. At lowest Strouhal number, 0·06, the maximum amplitude increases with density ratio with the largest increase, 53%, occurring between the lower density ratios. At the three higher Strouhal numbers, the maximum amplitudes increase on average about 12% as the density ratio changes from 0·5 to 1·0; however, as the density ratio is increased to 2·0, the maximum amplitude decreases slightly. Since these instability waves occur in the larger shear layer, they continue to grow downstream past the point at which the two shear layers merge. Thus, these results indicate the balance between the amount of initial instability wave growth and the amount of growth that occurs after the shear layers fully merge. For a density ratio of 0·5, the initial growth is less, since the inner shear layer has the highest spreading rate resulting in a lower maximum amplitude. For a density ratio of 2·0, the initial growth is comparable to that at a density ratio of 1·0; however, after the two shear layers fully merge, the density ratio 2·0 mean flow spreads more rapidly than the density ratio 1·0 mean flow, resulting in the local growth rates decreasing more rapidly at the higher Strouhal numbers for density ratio 2·0 than for the density ratio 1·0. Thus, the maximum amplitude is diminished for the $\rho_2/\rho_1 = 2{\cdot}0$ case as compared to the $\rho_2/\rho_1 = 1{\cdot}0$ case.

For the outer shear layer $n = 1$ instability waves, the maximum amplitudes are shown in Figure 14. Growing Kelvin–Helmholtz type instabilities were found only at the lower Strouhal numbers. The density ratio across the outer shear layer is decreasing as the

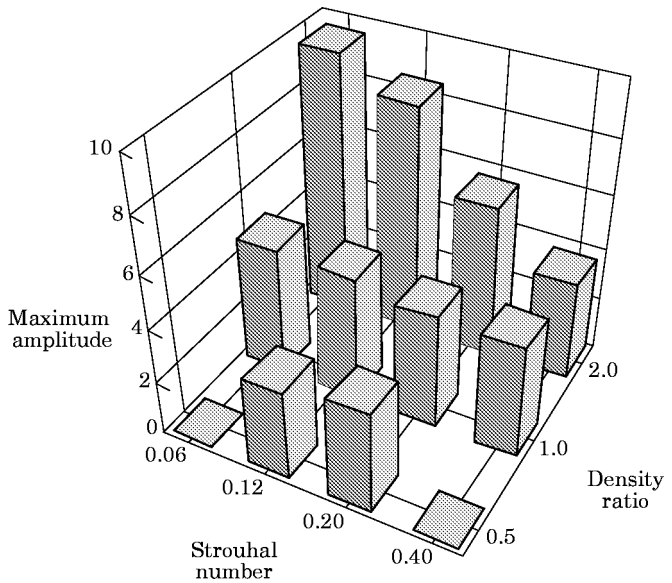

Figure 15. The effects of the density ratio and the Strouhal number on the maximum amplitude of instability waves in the outer shear layer: $n = 1$, $U_2/U_1 = 0{\cdot}6$, $AR = 1{\cdot}25$.

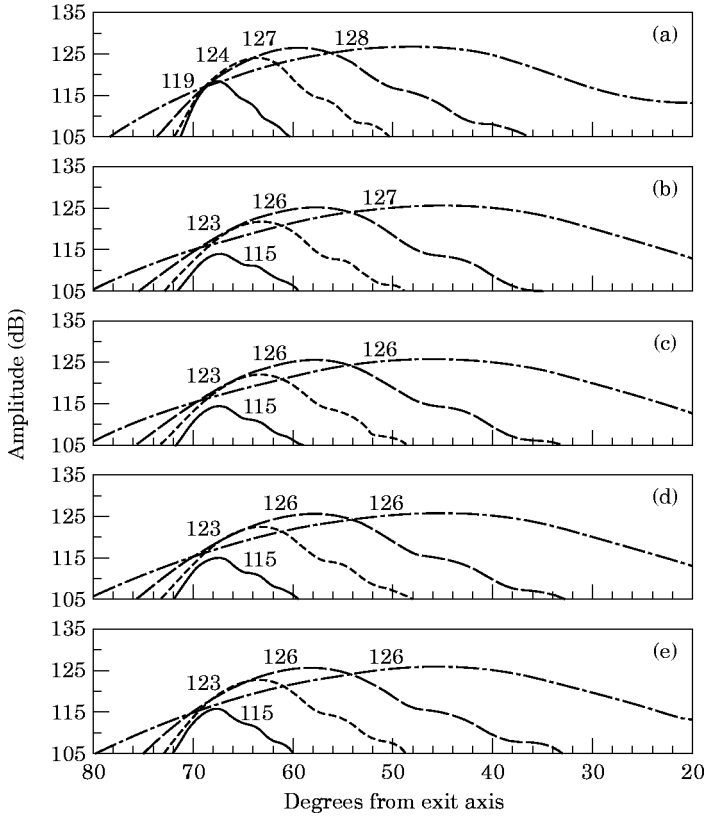

Figure 16. Far field directivity patterns for NVP jets with varying area ratio: $n = 1$, $U_2/U_1 = 0{\cdot}8$, $\rho_2/\rho_1 = 2{\cdot}0$, outer shear layer. Numbers indicate peak amplitudes. (a) Reference jet. The area ratio is (b) 1·25, (c) 1·00, (d) 0·75 and (e) 0·50. Strouhal numbers: — - — -, 0·06; — — —, 0·12; ----, 0·20; ——, 0·40.

indicated density ratio increases across the inner shear layer. This corresponds to a decrease in the outer shear layer spreading rate. In addition, since the outer shear layer is smaller than the inner shear layer, the outer shear layer instability waves are driven toward being damped before the two shear layers fully merge or, for higher Strouhal numbers, before the end of the outer potential core. Thus, the maximum amplitudes shown for the lower Strouhal numbers increase with a decrease in outer shear layer spreading rate (density ratio increasing) and, for the higher Strouhal number, the maximum amplitudes are affected by the rapid decrease in growth rates that occurs as the instability waves approach the end of the short outer potential cores.

For the second example, the velocity ratio is increased to 0·6, making the outer shear layer larger than the inner shear layer. The operating conditions are given in Table 1. The behavior of the operating conditions follows the same pattern as in the first example when the density ratio is changed but with lower Mach numbers for the inner stream and higher Mach numbers for the outer stream. The combination of an increase in the velocity ratio and corresponding changes in jet stream temperatures result in lower initial spreading rates in both shear layers compared to the spreading rates in the previous example. For the smaller inner shear layer, the lower initial growth rates for the instability waves, compared to the $U_2/U_1 = 0{\cdot}4$ case inner shear layer growth rates, are damped out as this shear layer merges with the larger outer shear layer, further lowering the maximum amplitude of the instability wave. This results in a set of maximum amplitudes as a function of the density

ratio and the Strouhal number that are similar in relative level to those shown in Figure 13, but with typically half the amplitude. The more important growing instability waves for this case are found in the larger outer shear layer. Here, the lower Strouhal number instability waves continue to grow beyond the end of the outer potential core and into the fully merged shear layer region. Thus, as shown in Figure 15, these instability waves obtain large relative maximum amplitudes especially for $\rho_2/\rho_1 \geqslant 1{\cdot}0$. Again, as in the previous example, the density ratio across the outer shear layer is decreasing as the density ratio across the inner shear layer increases, promoting a decrease in the outer shear layer spreading rate. This leads to higher instability wave amplitudes as the slowly spreading shear layer allows the wave to grow further downstream.

3.4. EFFECTS OF AREA RATIO

The general effect of decreasing the area ratio on the mean flow is to decrease the length of the outer potential core and to cause the two shear layers to merge faster. This would then affect the growth and decay of the instability waves and the resulting radiated noise. Two examples of the effects of area ratio changes on radiated noise are shown in Figures 16 and 18. In each figure are shown the relative amplitudes of the far field noise radiation patterns associated with four Strouhal numbers with the peak levels labelled on the figures. For a velocity ratio U_2/U_1 of 0·8, in Figure 16 it is shown that changing the area ratio has little impact on the relative levels of radiated noise from the instability waves in the outer shear layer. The velocity difference across the outer shear layer is much larger than that across the inner shear and the radiated noise from the outer shear layer instability waves dominates in the far field. As shown in Figure 17, the unchanging far field levels are due to similarities in the local growth rates of the instability waves in the large outer shear layer. The figure shows the location where the two shear layers begin to merge at the end of the outer potential core (vertical lines) as the area ratio changes. Even as the area ratio becomes smaller and the shear layers merge closer to the nozzle exit, the instability waves in the outer shear layer are not significantly affected by merging the smaller inner shear layer sooner with the much larger outer shear layer.

In contrast, in Figure 18 is shown what happens when the two shear layers have nearly the same velocity differences. Here, the velocity ratio is 0·4, making the inner shear layer velocity difference slightly larger than the outer shear layer velocity difference, resulting

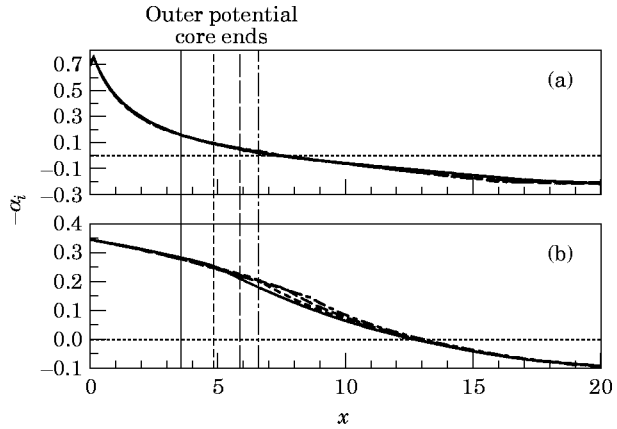

Figure 17. Instability wave local growth rates for NVP jets with a varying area ratio: $n = 1$, $U_2/U_1 = 0{\cdot}8$, $\rho_2/\rho_1 = 2{\cdot}0$, outer shear layer. Area ratio: — - — -, 1·25; — — —, 1·00, ----, 0·75; ———, 0·50. Strouhal number: (a) 0·40; (b) 0·06.

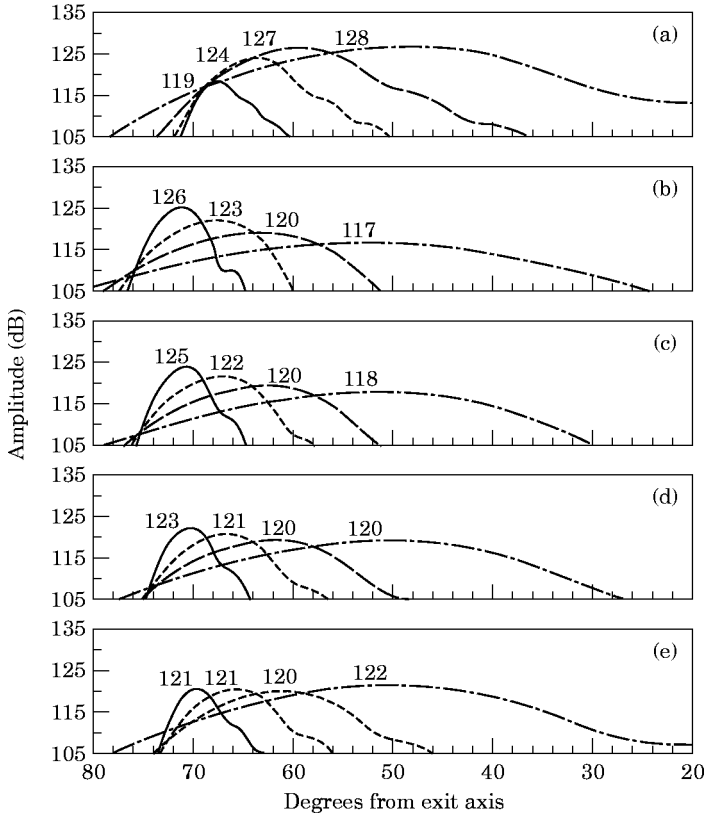

Figure 18. Far field directivity patterns for NVP jets with a varying area ratio: $n = 1$, $U_2/U_1 = 0{\cdot}4$, $\rho_2/\rho_1 = 2{\cdot}0$, inner shear layer. Numbers indicate peak amplitudes. See Figure 16 for legend.

in the inner shear instability wave dominating the outer shear layer instability wave. As the area ratio decreases, the lower Strouhal number far field amplitudes increase while the higher Strouhal number amplitudes decrease. The reason for this is shown in Figure 19. At a Strouhal number of 0·4, the local growth rate of the inner shear layer instability wave

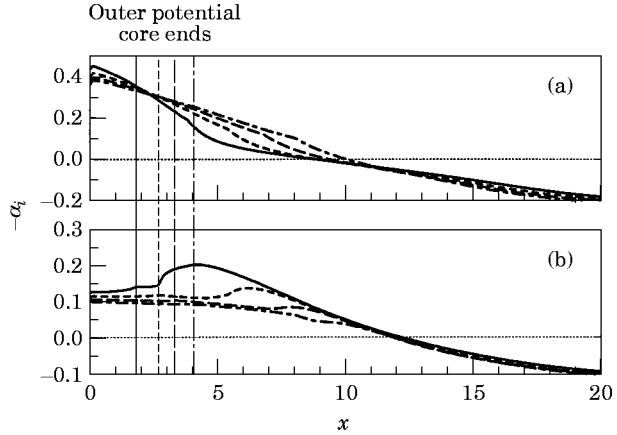

Figure 19. Instability wave local growth rates for NVP jets with a varying area ratio: $n = 1$, $U_2/U_1 = 0{\cdot}4$, $\rho_2/\rho_1 = 2{\cdot}0$, inner shear layer. See Figure 17 for legend.

decreases faster as the shear layers merge sooner with a decreasing area ratio. The larger downstream merging shear layer is unable to continue to support this shorter wavelength instability wave; its growth rate slows and it begins to decay sooner. In contrast, the growth rates for the longer wavelength, lower Strouhal number 0·06 case are enhanced by the earlier merging of the two shear layers. The instability wave grows to a higher amplitude before it begins to decay, a process that is governed by the single fully merged jet downstream.

4. CONCLUDING REMARKS

The noise generation from supersonic coaxial jets has been studied in this paper by extending the instability wave, noise generation model for single stream, axisymmetric jets to dual stream, coaxial jet. For high speed, perfectly expanded, axisymmetric jets, the instability waves or large scale coherent structures dynamically control the development of the free shear flow, and when the instability wave phase velocity exceeds the ambient speed of sound, these waves are the dominant source of mixing noise radiated into the downstream arc of the jet. Linear instability wave analysis is applied to the jet shear layer to obtain the characteristics that describe a growing and decaying instability wave and, subsequently, predict the radiated noise. These concepts, which have been applied to single jets with a single spreading shear layer, are now applied to a coaxial jet with two spreading shear layers.

The stability analysis was completed for a slowly diverging free jet shear layer with the assumption that the mean static pressure was constant. To lowest order inside the jet, the analysis resulted in an eigenvalue problem based on the compressible Rayleigh equation that gave local growth rates and phase velocities at each axial location as the mean flow developed. These local stability characteristics were used to calculate growing and decaying instability waves in the jet shear layers. Outside the jet, the instability wave was the source for near field pressure disturbances. For those instability wave components with supersonic phase velocities relative to ambient, the instability wave was the source of far field radiated noise. The results from stability calculations conducted for both single and coaxial supersonic jets in this study using numerically generated mean flow profiles compared favorably with the results from studies using analytical formulations to describe the mean flow.

Since the instability wave noise generation model lacks the ability to predict the absolute amplitude of the radiated noise, we are left to infer the effects of changes in operating conditions on radiated noise by how the growing instability waves are affected. With the initial amplitudes of the instability waves set to 1, we were assuming that the instability waves were generated by white noise at the nozzle exit. Thus, the relative levels of the different Strouhal number peaks of the far field directivity patterns followed the same relative level pattern as the maximum amplitudes of the instability waves that had peak components with supersonic phase velocities. The lower Strouhal numbers dominated in the outer shear layer and had directivity patterns with wide peaks. The higher Strouhal numbers dominated in the inner shear layer and had narrow peaks. The manipulation of operating conditions has shown that the peak levels of mixing noise radiated from the reference jet at lower Strouhal numbers and at angles of about 50 degrees to the jet exit axis could be shifted to higher Strouhal numbers and larger angles of about 70 degrees by using normal velocity profile jets. It would then be easier to reduce this higher frequency noise with a lined ejector shroud around the jet.

With the ability to numerically calculate mean flow profiles for NVP supersonic coaxial jets and to use those results to calculate the stability characteristics of both shear layers,

we conducted a parametric study of the effects of various operating conditions on the instability waves in and the subsequent noise generation from these jets. We focused on the effects of velocity ratio changes with a fixed density ratio of 1·0 and a fixed area ratio of 1·25. Next, we fixed the velocity and considered the effects of changes in density ratio. Finally, with both velocity and density ratios fixed, we varied the area ratio. Given that all the NVP jets have the same thrust, mass flow and exit area as a single reference jet, the following results were found for the stability characteristics:

(1) The stability characteristics for high speed NVP jets had the same trends as found in measurements of low speed NVP jets. For $U_2/U_1 < 0{\cdot}5$, the dominant instability was in the inner shear layer, and the higher amplitudes of these instabilities were at a higher frequency than the outer shear layer instability wave amplitudes. Conversely, for $U_2/U_1 > 0{\cdot}5$, the dominant outer shear layer instability wave maximum amplitudes had a lower frequency than those in the inner shear layer.

(2) For a given velocity ratio, the effect of the density ratio changes was to change the spreading rates of both shear layers. As the spreading rate decreased, there was a tendency for the instability wave to grow to a higher amplitude. However, in coaxial jets, the two shear layers merged together and modified the growth rate of the dominant instability. Results were shown where the maximum amplitude of the instability wave was diminished by the effects of merging (Figure 13) and where the maximum amplitude was enhanced (Figure 15) when the density ratio was increased from 1·0 to 2·0.

(3) The effect of area ratio changes was to cause the shear layers to merge closer to the nozzle exit as the area ratio decreased. If the velocity ratio was large, this had little impact on the growing instability wave when the large dominant shear layer merged with the smaller shear layer. When the velocity ratio was moderate in size, contradictory effects were found in the dominant instability waves of the larger shear layer. For lower Strouhal numbers, the earlier merging enhanced the growth rate. Conversely, for higher Strouhal numbers, the earlier merging diminished the growth rate.

REFERENCES

1. M. D. Dahl and P. J. Morris 1997 *Journal of Sound and Vibration* **200**, 701–719. Noise from supersonic coaxial jets, part 3: inverted velocity profile.
2. F. B. Greatrex 1961 *Society of Automotive Engineers Transactions* **69**, 312–324. By-pass engine noise.
3. T. J. Williams, M. R. M. H. Ali and J. S. Anderson 1969 *Journal of Mechanical Engineering Science* **11**, 133–142. Noise and flow characteristics of coaxial jets.
4. K. M. Eldred, V. Mason, E. Cuadra, R. Potter and J. Wilson 1971 *FAA FAA-RD*-71-101. Far field noise generation by coaxial flow jet exhausts, vol. 1—detailed discussion.
5. H. W. Dahlen 1972 *1st International Symposium on Air Breathing Engines*. Some experiments on the noise emission of coaxial jets.
6. W. Olsen and R. Friedman 1974 *NASA TM X*-71503. Jet noise from co-axial nozzles over a wide range of geometric and flow parameters.
7. H. K. Tanna 1980 *Journal of Sound and Vibration* **72**, 97–118. Coannular jets—are they really quiet and why?
8. H. K. Tanna and P. J. Morris 1985 *Journal of Sound and Vibration* **98**, 213–234. The noise from normal-velocity-profile coannular jets.
9. H. K. Tanna, W. H. Brown and C. K. W. Tam 1985 *Journal of Sound and Vibration* **98**, 95–113. Shock associated noise of inverted-profile coannular jets, part I: experiments.
10. J. R. Stone 1977 *NASA TM*-73838. An empirical model for inverted-velocity-profile jet noise prediction.
11. J. R. Stone, J. H. Goodykoontz and O. A. Gutierrez 1979 *NASA TM*-79095. Effects of geometric and flow-field variables on inverted-velocity-profile coaxial jet noise and source contributions.

12. J. R. Stone, D. E. Groesbeck and C. L. Zola 1983 *American Institute of Aeronautics and Astronautics Journal* **21**, 336–342. Conventional profile coaxial jet noise prediction.
13. S. P. Pao 1979 *NASA TP*-1301. A correlation of mixing noise from coannular jets with inverted flow profiles.
14. C. Y. Chen 1976 *AIAA Paper No*. 76-4. A model for predicting aero-acoustic characteristics of coaxial jets.
15. T. F. Balsa and P. R. Gliebe 1977 *American Institute of Aeronautics and Astronautics Journal* **15**, 1550–1558. Aerodynamics and noise of coaxial jets.
16. P. R. Gliebe and T. F. Balsa 1978 *Journal of Aircraft* **15**, 743–749. Aeroacoustics of axisymmetric single- and dual-flow exhaust nozzles.
17. P. R. Gliebe, J. F. Brausch, R. K. Majjigi and R. Lee 1991 *Aeroacoustics of Flight Vehicles*: *Theory and Practice Volume* 2: *Noise Control*, *NASA RP*-1258. See Chapter 15: Jet noise suppression.
18. C. K. W. Tam 1991 *Aeroacoustics of Flight Vehicles*: *Theory and Practice Volume* 1: *Noise Sources*, *NASA RP*-1258. See Chapter 6: Jet noise generated by large-scale coherent motion.
19. N. W. M. Ko and A. S. H. Kwan 1976 *Journal of Fluid Mechanics* **73**, 305–332. The initial region of subsonic coaxial jets.
20. A. S. H. Kwan and N. W. M. Ko 1976 *Journal of Sound and Vibration* **48**, 203–219. Coherent structures in subsonic coaxial jets.
21. A. S. H. Kwan and N. W. M. Ko 1977 *Journal of Fluid Mechanics* **82**, 273–287. The initial region of subsonic coaxial jets, part 2.
22. W. J. A. Dahm, C. E. Frieler and G. Tryggvason 1992 *Journal of Fluid Mechanics* **241**, 371–402. Vortex structure and dynamics in the near field of a coaxial jet.
23. T. R. S. Bhat and J. M. Seiner 1993 *AIAA Paper No*. 93-4410. The effect of velocity profiles on supersonic jet noise.
24. H. K. Tanna 1977 *Journal of Sound and Vibration* **50**, 429–444. An experimental study of jet noise, part II: shock associated noise.
25. H. K. Tanna, W. H. Brown and C. K. W. Tam 1981 *NASA CR*-3454. Shock associated noise reduction from inverted-velocity-profile coannular jets.
26. C. K. W. Tam and D. E. Burton 1984 *Journal of Fluid Mechanics* **138**, 273–295. Sound generated by instability waves of supersonic flows, part 2: axisymmetric jets.
27. M. Gaster, E. Kit and I. Wygnanski 1985 *Journal of Fluid Mechanics* **150**, 23–39. Large-scale structures in a forced turbulent mixing layer.
28. R. A. Petersen and M. M. Samet 1988 *Journal of Fluid Mechanics* **194**, 153–173. On the preferred mode of jet instability.
29. C. K. W. Tam and P. J. Morris 1985 *Journal of Sound and Vibration* **102**, 119–151. Tone excited jets, part V: a theoretical model and comparison with experiment.
30. P. J. Morris, M. G. Giridharan and G. M. Lilley 1990 *Proceedings of the Royal Society of London*, *Series A* **431**, 219–243. On the turbulent mixing of compressible free shear layers.
31. M. D. Dahl and P. J. Morris 1997 *Journal of Sound and Vibration* **200**, 643–663. Noise from supersonic coaxial jets, part 1: mean flow predictions.
32. C. K. W. Tam, P. Chen and J. M. Seiner 1992 *American Institute of Aeronautics and Astronautics Journal* **30**, 1747–1752. Relationship between instability waves and noise of high-speed jets.
33. J. M. Seiner, T. R. S. Bhat and M. K. Ponton 1993 *AIAA Paper No*. 93-0734. Mach wave emission from a high temperature supersonic jet.
34. C. K. W. Tam and F. Q. Hu 1989 *Journal of Fluid Mechanics* **201**, 447–483. On the three families of instability waves of high-speed jets.
35. C. K. W. Tam and D. E. Burton 1984 *Journal of Fluid Mechanics* **138**, 249–271. Sound generated by instability waves of supersonic flows, part 1: two-dimensional mixing layers.
36. D. E. Burton 1981 *Ph.D. Dissertation*, *Florida State University*. Application of the method of matched asymptotic expansions to large scale instability wave and sound radiation problems of axisymmetric jets.
37. M. D. Dahl 1994 *Ph.D Dissertation*, *Penn State University*. The aeroacoustics of supersonic coaxial jets.
38. C. K. W. Tam 1989 *AIAA Paper No*. 89-1088. Forward flight effects on broadband shock associated noise of supersonic jets.
39. G. B. Whitham 1974 *Linear and Nonlinear Waves*. New York: Wiley-Interscience.
40. C. K. W. Tam and P. J. Morris 1980 *Journal of Fluid Mechanics* **98**, 349–381. The radiation of sound by the instability waves of a compressible plane turbulent shear layer.
41. M. Van Dyke 1975 *Perturbation Methods in Fluid Mechanics*. Stanford, CA: Parabolic Press.

42. C. M. Bender and S. A. Orszag 1978 *Advanced Mathematical Methods for Scientists and Engineers*. New York: McGraw-Hill.
43. R. B. Dingle 1973 *Asymptotic Expansions*: *their Derivation and Interpretation*. New York: Academic Press.
44. C. K. W. Tam and P. Chen 1993 *AIAA Paper No*. 93-4408. Turbulent mixing noise from supersonic jets.
45. P. J. Morris and T. R. S Bhat 1992 *DGLR/AIAA Paper No*. 92-02-042. The noise from supersonic elliptic jets.
46. M. C. Junger and D. Feit 1986 *Sound*, *Structures*, *and Their Interactions*. Cambridge, MA: The MIT Press; second edition.
47. A. D. Pierce 1989 *Acoustics*. Woodbury, NY: Acoustical Society of America.
48. L. M. Mack 1984 *Special Course on Stability and Transition of Laminar Flow*, *AGARD-R*-709. Boundary-layer linear stability theory.
49. P. G. Drazin and W. H. Reid 1981 *Hydrodynamic Stability*. Cambridge: Cambridge University Press.
50. G. W. Stewart 1973 *Introduction to Matrix Computations*. New York: Academic Press.
51. C. K. W. Tam 1975 *Journal of Sound and Vibration* **38**, 51–79. Supersonic jet noise generated by large scale disturbances.
52. P. J. Morris and C. K. W. Tam 1977 *AIAA Paper No*. 77-1351. Near and far field noise from large-scale instabilities of axisymmetric jets.
53. J. P. Boyd 1985 *Journal of Computational Physics* **57**, 454–471. Complex coordinate methods for hydrodynamic instabilities and Sturm–Liouville eigenproblems with an interior singularity.
54. E. O. Brigham 1974 *The Fast Fourier Transform*. Englewood Cliffs, N.J.: Prentice-Hall.
55. E. G. Williams and J. D. Maynard 1982 *Journal of the Acoustical Society of America* **72**, 2020–2030. Numerical evaluation of the Rayleigh integral for planar radiators using the FFT.
56. W. A, Veronesi and J. D. Maynard 1987 *Journal of the Acoustical Society of America* **81**, 1307–1322. Nearfield acoustic holography (NAH) II: holographic reconstruction algorithms and computer implementation.
57. J. M. Seiner, M. K. Ponton, B. J. Jansen and N. T. Lagen 1992 *DGLR/AIAA Papper No*. 92-02-046. The effects of temperature on supersonic jet noise emission.
58. M. D. Dahl and P. J. Morris 1995 *NASA TM*-106872. Supersonic jet noise reductions predicted with increased jet spreading rate.
59. A. Michalke 1984 *Progress in Aerospace Sciences* **21**, 159–199. Survey of jet instability theory.
60. A. Michalke and G. Hermann 1982 *Journal of Fluid Mechanics* **114**, 343–359. On the inviscid instability of a circular jet with external flow.
61. E. Gutmark, K. C. Schadow and K. J. Wilson 1991 *Physics of Fluids A* **3**, 29–36. Effect of convective mach number on mixing of coaxial circular and rectangular jets.